공학박사 학위논문

전기차용 황화물 전해질기반 전고체전지 양극 계면에 관한 연구

Study on the cathode interface in all-solid-state batteries employing sulfide electrolytes for electric vehicles

2023 년 2 월

서울대학교 대학원

재료공학부

윤 경 호

전기차용 황화물 전해질기반 전고체전지 양극 계면에 관한 연구

Study on the cathode interface in all-solid-state batteries employing sulfide electrolytes for electric vehicles

지도 교수 강 기 석

이 논문을 공학박사 학위논문으로 제출함

2022 년 12 월

서울대학교 대학원
재료공학부
윤 경 호

권기윤 의 박사 학위논문을 인준함

2022 년 12 월

위원장	임종우	(인)
부위원장	강기석	(인)
위원	김영준	(인)
위원	김한수	(인)
위원	정윤석	(인)

Abstract

Study on the cathode interface in all-solid-state batteries employing sulfide electrolytes for electric vehicles

Yoon, Kyungho

Department of Materials Science and Engineering

College of Engineering

The Graduate School

Seoul National University

Among energy storage systems, rechargeable lithium-ion batteries have been the most successful battery system for small electronic devices for decades owing to their low cost, high energy density, power capability and stable cyclability. As the application of battery system has extended from small electronic devices to large electronic devices such as electric vehicles (EVs), finding safe and energy-dense batteries has become crucial mission. In particular, presence of organic liquid electrolyte in traditional lithium ion rechargeable batteries endangers safety of the users by explosion, which will be life-threatening in case of large-scale batteries.

Today, all-solid-state batteries (ASSBs) employing non-flammable solid electrolytes are considered as one of the most promising candidates for electric vehicles with respect to the safety. Extensive search for novel solid electrolytes with high ionic conductivity has been carried out for the past decades in the development of ASSBs. Among them, recent discovery of sulfide-based electrolytes has invigorated the field, as the ionic conductivity could reach the similar level to that of the commercial organic liquid electrolytes. Moreover, the malleable mechanical nature of the sulfides generally offers reasonably good physical contact with other components in the electrode, alleviating large contact resistance between the solid components. Hence, the rapid development of high-energy-density ASSBs in recent years through extensive research efforts—by leveraging the high-capacity lithium metal and the versatile form factor—further expedites the potential implementation of ASSB in large-scale EVs. However, in order to successfully mount ASSBs in EVs, achieving high-power density for fast-charging and examining calendar aging properties at different temperatures will be central mission. In this thesis, I present issues on the composite cathode interface in all-solid-state batteries when all-solid-state batteries employing sulfide electrolytes are design for high-power density and are exposed to calendar aging at wide range of storage temperatures.

In chapter 2, I raise the dilemma in constructing ASSBs concerning the conductive agent, which provides the electronic pathway but simultaneously promotes the degradation of the sulfide electrolytes. I found out that inclusion of carbon additives in composite cathode induces a large polarization during charging and discharging, followed by the decreased initial capacity along with an unusual voltage slope at around 2.6 V vs Li/Li^+. Furthermore, I found out that the degradation of the electrochemical performance of the carbon-containing cathode composite is correlated with the severe impedance increase at the cathode interface during cycles. Therefore, optimizing amount of carbon conductive agents or finding a suitable conductive agent with a minimal influence on the electrolyte is essential in designing high power density ASSBs employing sulfide electrolytes.

In chapter 3, I examined the calendar aging properties of the most representative ASSB system comprising of Li_6PS_5Cl solid electrolyte and commercial $LiNi_{0.8}Co_{0.1}Mn_{0.1}O_2$ (NCM811) cathode, mimicking the practical storage conditions of EVs in varying outdoor conditions. It is carefully examined how the performance of ASSB is retained/altered when exposed to (i) outdoor temperatures (*e.g.*, -20 °C, 20 °C and 70 °C), (ii) for an extended rest period, and (iii) at a charged state, in comparisons to the conventional LIBs. My results reveal that the Li_6PS_5Cl-NCM811 ASSB can retain its performance remarkably well at low temperatures, which excels the calendar aging properties of equivalent lithium cells containing liquid electrolyte. On the other hand, a substantial deterioration of ASSB is observed after the storage at high temperature, which is accompanied by a significant increase in the overpotential and the decrease in the capacity to almost less than a half of the deliverable capacity, making a clear contrast to the reference lithium cells employing the liquid electrolyte. In conclusion, my thesis suggests that future research efforts should be placed in developing effective strategies to

overcome various issues with ASSBs in real-world environments in order to successfully mount ASSBs in EVs.

Keywords : Energy storage, Batteries, all-solid-state batteries, composite cathode interfaces, sulfide electrolytes

Student Number : 2016-20805

Table of Contents

List of Figures

Figure 2-6. Electrochemical impedance spectrum of ASSB after 10 cycles at 0.075C with various weight ratios of Super P. (a) Electrochemical impedance spectrum of ASSB after 2 cycles at 0.075C with various weight ratios of Super P. (b) Impedance spectrum of 0 wt. % Super P after 2, 6 and 10 cycles. (c) Impedance spectrum of 3 wt. % Super P after 2, 6 and 10 cycles. (d) Impedance spectrum of 5 wt. % Super P after 2, 6 and 10 cycles. Areas of semi-circles are calculated and displayed on the figure. All electrochemical impedance tests were performed in room temperature.

Figure 2-7. Electrochemical impedance spectra of 5 wt.% Super P containing ASSB after various rest time. The inset graph is the magnification of initial electrochemical impedance spectra of ASSB with 5 wt.% Super P.

Figure 2-8. Deconvoluted S 2p XPS spectra of composite cathodes. (a) Top panel: Deconvoluted S 2p XPS spectra of pristine carbon-free composite cathode. Bottom panel: Deconvoluted S 2p XPS spectra of first charged carbon-free composite cathode. (b) Top panel: Deconvoluted S 2p XPS spectra of pristine 5 wt. % carbon-containing composite cathode. Bottom panel: Deconvoluted S 2p XPS spectra of first charged 5 wt. % carbon-containing composite cathode.

Figure 2-9. Carbon XPS spectra of composite cathode with 5 wt. % Super P before and after charging process.

Figure 2-10. Cycle performance of all-solid-state battery with/without carbon additives in composite cathode. The ASSB with carbon additive (Super P) shows not only decreased initial discharge capacity but also unstable cycle life of ASSB compared to carbon-free ASSB. While capacity of carbon-free ASSB is steadily maintained about 125 mAh g^{-1}, capacity of 5 wt. % Super P-containing ASSB is unstable throughout 35 cycles.

Figure 2-11. Electrochemical profile of 5 wt. % Super P-containing ASSB. Electrochemical profile of 5 wt. % Super P-containing ASSB for initial three cycles is shown. The additional slope in charging step is only observed in first charging process.

Figure 3-1. Voltage profiles of solid-state cells and liquid electrolyte cells employing NCM811 at various storage temperatures. a) Second charge curves of solid-state cells before storage conditions and subsequent discharge curves after three different storage temperatures. b) Second charge curves of liquid electrolyte cells before storage conditions and subsequent discharge curves after three different storage temperatures.

Figure 3-2. X-ray diffraction and Rietveld refinement of NCM811 and Li_6PS_5Cl. a) Rietveld refinement plot showing the observed (black) and calculated (red) diffraction data and their difference (blue) for NCM811. b) Rietveld refinement plot showing the observed (black) and calculated (red) diffraction data and their difference (blue) for Li_6PS_5Cl.

Figure 3-3. Warburg factor and Li diffusion coefficient. D_{Li+} value is plotted in terms of A, assuming n and C values are equal to 1 for simple calculation.

Figure 3-4. SEM images of NCM811 cathode active materials. a) low magnification SEM image of NCM811. b) high magnification SEM image of NCM811.

Figure 3-5. Voltage profiles and cycle life of solid-state cells and liquid electrolyte cells employing NCM811 after exposure to various storage temperatures. (a) Third charge/discharge curves of all-solid-state batteries after four different storage conditions: no storage, six days of storage at −20, 20, and 70 °C. (b) Third charge/discharge curves of liquid electrolyte batteries after four different storage conditions: no storage, 4.3 V charged solid-state cells from six days of storage at −20, 20, and 70 °C. (c) Cycle life of solid-state cells after exposure to four different storage conditions. (d) Cycle life of liquid electrolyte cells after exposure to four different storage conditions.

Figure 3-6. Differential capacity curves and electrochemical impedance spectra of 4.3 V charged solid-state cells in various storage temperatures. (a) dQ/dV graph of a solid-state cells at third cycle without storage. (b) dQ/dV graph of a solid-state cells at third cycle stored in −20 °C. (c) dQ/dV graph of a solid-state cell at third cycle stored in 20 °C. (d) dQ/dV graph of a solid-state cell at third cycle stored in 70 °C. (e) Electrochemical impedance spectra of −20, 20, and 70 °C stored solid-state cells. (f) Designated resistance values based on equivalent circuit of solid-state cells. R_{CC}, R_{SE}, R_{AI}, and R_{CI} refer to resistance of current collector, solid electrolyte, anode interface, and cathode interface, respectively.

Figure 3-7. Differential capacity curves and electrochemical impedance spectra of 4.3 V charged liquid electrolyte batteries in various storage temperatures. a) dQ/dV graph of a liquid electrolyte cell at third cycle without storage. b) dQ/dV graph of a liquid electrolyte cell at third cycle stored in −20 °C. c) dQ/dV graph of a liquid electrolyte cell at third cycle stored in 20 °C. d) dQ/dV graph of a liquid electrolyte cell at third cycle stored in 70 °C. e) Electrochemical impedance spectra of liquid electrolyte cells stored at −20, 20 and 70 °C for six days. f) Equivalent circuit of liquid electrolyte cells. R_{LE}, R_{CEI} and R_{CT} refer to resistance of liquid electrolyte, solid electrolyte, cathode electrolyte interface and charge transfer, respectively.

Figure 3-8. X-ray diffraction analysis of 4.3 V charged all-solid-state battery stored under 20 and 70 °C. (a) XRD analysis of 4.3 V charged solid-state cells from zero to six days storage under 20 °C. Filled downward triangle and open diamond symbols refer to Li_6PS_5Cl and holder, respectively. (b) XRD analysis of 4.3 V charged solid-state cells from zero to six days of storage under 70 °C. Filled downward triangles, open downward triangles, open diamonds, filled diamonds, and open circle symbols refer to Li_6PS_5Cl, Li_3PS_4, holder, LiCl, and S, respectively. (c) (003) peak shift of 4.3 V charged NCM811 from zero to six days of storage under 20 °C ($2\theta = 18–20$). (d) Main peak shift of Li_6PS_5Cl from zero to six days of storage under 20 °C ($2\theta = 24–36$). (e) 003 peak shift of 4.3 V charged NCM811 from zero to six days of storage under 70 °C ($2\theta = 18–20$). (f) Main peak decomposition of Li_6PS_5Cl from zero to six days of storage under 70 °C ($2\theta = 24–36$).

Figure 3-9. X-ray Diffraction analysis of 4.3 V charged all-solid-state battery stored under –20 °C. a) XRD analysis of 4.3 V charged solid-state cells from 0 to 6 days storage under –20 °C. b) (003) peak shift of 4.3V charged NCM811 from 0 to 6 days storage under –20 °C (2θ = 18 – 20). c) Main peak shift of Li_6PS_5Cl from 0 to 6 days storage under –20 °C (2θ = 24 – 36).

Figure 3-10. *Ex-situ* XRD of NCM811 solid-state cells in operation voltage window of 3.0 – 4.3 V. (a) *ex-situ* XRD analysis of NCM811 solid-state cells at 0.1 C rate. b) (003) peak shift of NCM811 solid-state cells from pristine to 4.3 V (2θ = 18 – 20). c) Main peak shift of Li_6PS_5Cl from pristine to 4.3 V (2θ = 24 – 36).

Figure 3-11. X-ray diffraction analysis and polarization examination of 4.3 V charged Li_6PS_5Cl stored under 20 and 70 °C. (a) Schematics of experiments related to 4.3 V charged Li_6PS_5Cl. (b) XRD analysis of 4.3 V charged Li_6PS_5Cl stored under 20 and 70 °C for six days. (c) Second charge/discharge profiles of reference cell, 4.3 V charged Li_6PS_5Cl stored under 20 and 70 °C reassembled cells.

Figure 3-12. XANES spectra and morphology change followed by gas evolution of 4.3 V charged all-solid-state batteries stored under various temperatures. (a) XANES at sulfur Kedge spectra of 4.3 V charged solid-state cells stored under –20, 20, and 70 °C. (b) XANES spectra at phosphorus K-edge of 4.3 V charged solid-state cells stored under –20, 20, and 70 °C. (c) XANES spectra at chlorine K-edge of 4.3 V charged solid-state cells stored under – 20, 20, and 70 °C. (d) TGA-MS graph for 4.3 V charged NCM811 composite cathode showing relative sample mass loss, mass loss rate, heat flow, and ion current on m/z = 48 and m/z = 64. (e) SEM image of 4.3 V charged NCM811 composite cathode stored at –20 °C for six days. (f) SEM image of 4.3 V charged NCM811 composite cathode stored at 20 °C for six days. (g) SEM image of 4.3 V charged NCM811 composite cathode stored at 70 °C for six days

Figure 3-13. Electrochemical performance of ASSBs operating at 20 and 70 °C. a) First cycle profile of ASSBs operating at 0.1 C under 20 and 70 °C. b) Partially vacuumed ASSB package at pristine state. c) Dropped vacuum level of ASSB package after 20 cycles under 70 °C operating temperature. d) Cycle life of ASSBs at 0.1 C under 20 and 70 °C operating temperatures.

Figure 3-14. Electrochemical performance of ASSBs operating at 20 and 70 °C. a) Partially vacuumed 4.2 V charged ASSB package before 70 °C-storage. b) Dropped vacuum level of 4.2 V charged ASSB package after 6 days of 70 °C-storage c) Third cycle charge/discharge profile of 4.3 V charged ASSBs after 20 and 70 °C-storage for six days. d) Cycle life of ASSBs at 0.1 C under 20 and 70 °C.

Figure 3-15. SEM images of composite cathode in solid-state cells stored at –20 °C and 70 °C after 10 cycles. a–b) 4.3V charged NCM811 composite cathode stored at –20 °C for six days after 10 cycles. c–d) 4.3V charged NCM811 composite cathode stored at 70 °C for six days after 10 cycles. All samples are stored under vacuum/Ar atmosphere.

Figure 3-16. **Cross-section SEM images of 4.3 V charged NCM811 composite cathode stored at a) -20 and b) 70 °C.**

List of Tables

Chapter 1. Introduction

1.1 Motivation and outline

Against the imminent global climate change, vehicle electrification is now at the heart of the decarbonization pathway[1]. The growing success of electric vehicles (EVs) has been achieved with the rapid development of electrochemical storage technology represented by rechargeable lithium-ion batteries[1,2]. In fact, the electric vehicle world sales data base reported that the global market share of EVs, which was only 0.2% in 2012, has dramatically increased to 9% in 2021.[3] For further successful expansion of EV market, a significant breakthrough is needed in current battery technologies in terms of energy storage capacity, power capability, safety, and cost[4].

Among the battery issues to improve, safety issue became one of the most significant problem in its employment in new large-scale applications. Fabrication defects or the misuse of lithium ion batteries (LIBs) can cause catastrophic thermal runaway reactions involving the combustion of constituting organic liquid electrolytes, thereby leading to battery explosion.[5] In fact, a few recent safety incidents of EVs were found to be related to the instability of LIBs, which underscores the need for safer alternative batteries.[6] In this respect, ASSBs employing non-flammable solid electrolytes are considered as one of the most promising candidates for EVs.[7,8] Among the ASSBs, ASSBs employing sulfide solid electrolytes are considered as the closest ASSB system to industrialization due to their high ionic conductivity, favorable physical contact with electrodes, composition of light elements and facile pouch cell manufacture.[9-12] Although ASSBs employing sulfide electrolytes harbor great potential to be successful energy storage system for large electronic devices such as EVs, there are practical issues that need to be addressed.

First, ASSBs for EVs should not only deliver high energy density but also provide high power density, since EVs should easily yield speed up to about 200 km per hour, a comparable speed to that of gasoline cars. In LIB system, various types of carbon conductive agents are often added to provide facile electronic conduction in cathode in order to build high power density.[13-16] **In chapter 2**, I raise the dilemma in constructing ASSBs concerning the conductive agent, which provides the electronic pathway but simultaneously promotes the degradation of the sulfide electrolytes. I found out that introduction of carbon additives in composite cathode induces a large polarization during charging and discharging, followed by the decreased initial capacity along with an unusual voltage slope at around 2.6 V vs Li/Li^+. Moreover, I found out that the degradation of the electrochemical performance of the carbon-containing cathode composite is correlated with the severe impedance increase at the cathode interface during cycles. Therefore, optimally balancing them or finding a suitable conductive agent with a minimal influence on the electrolyte is essential in designing high power density ASSBs employing sulfide electrolytes.

Second, when considering batteries for EVs, one of the notable aspects that differ from the use in small electronic devices is their distinct operation conditions. Batteries in typical electronic devices such as cell phones undergo relatively moderate temperature variation, and only experience constant modes of either charge or discharge. On the other hand, batteries employed in EVs are expected to be exposed to a wider temperature variation due to their outdoor storage. Moreover, the intermittent usage/parking of these vehicles makes the batteries kept at rest in charged states for most of the time without being used. It implies that calendar aging properties of batteries at different states of charges (SOC) would be one of the most decisive factors in securing the reliability of battery systems in EVs under varying outdoor environments. Nevertheless, it is still elusive, to the best of our knowledge, how the storage capability of ASSBs would be affected by hot or cold weather for a practically long time with regards to their SOCs, although ASSBs are emphasized as the imminent alternative system for EV applications.[17-20] **In chapter 3,** I investigated the calendar aging properties of the most representative ASSB system comprising of Li_6PS_5Cl solid electrolyte and commercial $LiNi_{0.8}Co_{0.1}Mn_{0.1}O_2$ (NCM811) cathode, mimicking the practical storage conditions of EVs in varying outdoor conditions. It is carefully examined how the performance of ASSB is retained/altered when exposed to (i) outdoor temperatures (*e.g.*, -20 °C, 20 °C and 70 °C), (ii) for an extended rest period (up to a maximum of six days), and (iii) at a charged state (~ 4.3 V), in comparisons to the conventional LIBs. My results reveal that the Li_6PS_5Cl-NCM811 ASSB can retain its performance remarkably well at low temperatures, which excels the calendar aging properties of equivalent lithium cells containing liquid electrolyte. On the other hand, a substantial deterioration of ASSB is observed after the storage at high temperature, which is accompanied by a significant increase in the overpotential and the decrease in the capacity to almost less than a half of the deliverable capacity, making a clear contrast to the reference lithium cells employing the liquid electrolyte.

1.2 References

1. Cano, Z. P. *et al.* Batteries and fuel cells for emerging electric vehicle markets. *Nature Energy* **3**, 279 (2018).
2. Li, W., Erickson, E. M. & Manthiram, A. High-nickel layered oxide cathodes for lithium-based automotive batteries. *Nature Energy* **5**, 26 (2020).
3. IEA (2020), Global EV Outlook 2020, IEA, Paris https://www.iea.org/reports/global-ev-outlook-2020
4. Kwade, A. *et al.* Current status and challenges for automotive battery production technologies. *Nature Energy* **3**, 290 (2018).
5. Hess, S., Wohlfahrt-Mehrens, M. & Wachtler, M. Flammability of Li-Ion Battery Electrolytes: Flash Point and Self-Extinguishing Time Measurements. *J. Electrochem. Soc.* **162**, A3084 (2015).
6. Guirong, Z. and Henghai, Z. Research of the electric vehicle safety. *World Autom. Congr.*, 1 (2012).
7. Xiayin, Y. *et al.* All-solid-state lithium batteries with inorganic solid electrolytes: Review of fundamental science. *Chin. Phys. B* **25**, 018802 (2016).
8. Kim, J.-J., Yoon, K., Park, I. & Kang, K. Progress in the Development of Sodium-Ion Solid Electrolytes. *Small Methods* **1**, 1700219-n/a (2017).
9. Kamaya, N. *et al.* A lithium superionic conductor. *Nat. Mater.* **10**, 682 (2011).

10. Sakuda, A., Hayashi, A. & Tatsumisago, M. Sulfide Solid Electrolyte with Favorable Mechanical Property for All-Solid-State Lithium Battery. *Sci. Rep.* **3**, 2261 (2013).

11. Hayashi, A. *et al.* Preparation of Li_2S–P_2S_5 Amorphous Solid Electrolytes by Mechanical Milling. *J. Am. Ceram. Soc.* **84**, 477 (2001).

12. Sakuda, A., Hayashi, A. & Tatsumisago, M. Sulfide Solid Electrolyte with Favorable Mechanical Property for All-Solid-State Lithium Battery. *Sci. Rep.* **3**, 2261 (2013).

13. Spahr, M. *et al.* Development of carbon conductive additives for advanced lithium ion batteries. *J. Power Sources* **196**, 3404 (2011).

14. Qi, X. *et al.* Understanding the influence of conductive carbon additives surface area on the rate performance of $LiFePO_4$ cathodes for lithium ion batteries. *Carbon* **64**, 334 (2013).

15. Bauer, W. *et al.* Influence of dry mixing and distribution of conductive additives in cathodes for lithium ion batteries. *J. Power Sources* **288**, 359 (2015).

16. Chew, S. *et al.* Flexible free-standing carbon nanotube films for model lithium-ion batteries. *Carbon* **47**, 2976 (2009).

17. Whiteley, J. M. *et al.* Empowering the lithium metal battery through a silicon-based superionic conductor. *J. Electrochem. Soc* **161**, A1812 (2014).

18. Liang, B. *et al.* Preparation and characterization of PEO-PMMA polymer composite electrolytes doped with nano-Al2O3. *Electrochim. Acta* **169**, 334 (2015).

19. Wenzel, S. *et al.* Interphase formation and degradation of charge transfer kinetics between a lithium metal anode and highly crystalline $Li_7P_3S_{11}$ solid electrolyte. *Solid State Ion.* **286**, 24 (2016).

20. Ma, J. *et al.* Progress and prospect on failure mechanisms of solid-state lithium batteries. *J. Power Sources* **392**, 94 (2018).

Chapter 2. Investigation on the interface between $Li_{10}GeP_2S_{12}$ electrolyte and carbon conductive agents in all-solid-state lithium battery

(The content of this chapter has been published in Sci. *Rep.* [Yoon, K., Kim, J. *et al.*, *Sci. Rep.* **2018**, 8, 8066.]-Reproduced by permission of Nature Publishing Group)

2.1 Introduction

A development of safe and reliable energy storage has been re-highlighted with the recent incidents involving battery swelling/burning and subsequent recall of the lithium ion batteries.[1,2] In particular, with the lithium-ion battery technology being actively incorporated into electric vehicles and large-scale energy storage systems, the safety of the large-size batteries cannot be overstated. The organic liquid electrolyte used in conventional lithium-ion batteries usually acts as a fuel for the combustion in a thermal-runaway reaction, thereby leading to safety incidents.[3] On the other hand, ASSBs exploit non-flammable solid electrolytes, making them much more tolerant to reactions with such explosive natures, thus are regarded as the promising safe alternative to the current lithium-ion batteries.[4-6] However, employing solid-state electrolyte in the ASSBs accompanies several important technical issues that need to be addressed such as the necessity of finding solid-state fast ionic conductors whose ionic conductivity should be comparable to that of the liquid electrolyte and the careful interface control of the solid-solid contacts among the various components in the battery.[7-9]

Extensive search for novel solid electrolytes with high ionic conductivity has been carried out for the past decades in the development of ASSBs.[8,10-12] Among them, recent discovery of sulfide-based electrolyte including LGPS has invigorated the field, as the ionic conductivity could reach the similar level to that of the commercial organic liquid electrolytes.[8] Moreover, the malleable mechanical nature of the sulfides generally offer a good physical contact with other components in the electrode, alleviating the unnecessarily large contact resistance between the solid components.[13] Notable is that typical oxides-based solid electrolytes generally require a high-temperature sintering to reduce the abnormally large contact resistance, thus offering limited options for cell configurations.[14-19] Nevertheless, the construction of reliable ASSBs using sulfide electrolytes still faces several technical challenges.[20-22] One of the critical bottlenecks is to effectively maintain the interface stability between the electrode and the solid electrolyte in terms of not only the physical contact but also the chemical stability. For example, S. Wenzel *et al.* reported that chemical reactions at Li/LGPS interface leads to the decomposition of LGPS, producing an undesirable interphase composed of Li_3P, Li_2S, and Li-Ge alloy.[20] A. Sakuda *et al.* also revealed that an interfacial layer was formed after initial charge of the battery due to the mutual diffusion of Co, P, and S at the interface between $LiCoO_2$ and Li_2S-P_2S_5.[21] In this regard, various surface modifications and protections of electrode materials in ASSBs have been conducted in order to decrease the side reaction at the interface with the solid electrolyte.[23-28]

In a practical cell configuration, conductive agents are inevitable in the electrode fabrication to aid in the electronic conduction throughout the electrode. In ASSBs, thus, not only the interface between the solid electrolyte and the electrode material, but also that with the conductive agents have to be carefully investigated. While several studies showed that ASSBs based on LGPS electrolyte without carbon additives could exhibit first discharge capacity near the theoretical capacity of $LiCoO_2$ with relatively stable cycle life,[29] such electrochemical cycling was possible because $LiCoO_2$ becomes metallic after delithiation, and was examined at relatively slow current rate (~0.1C).[8,29,30] In order to achieve reasonably high power density and for the adoption of other cathode materials that are generally not metallic in ASSBs, the inclusion of conductive agents such as carbon additives in composite cathodes is unavoidable. Moreover, one of the recent studies by Han *et al.* further motivated us to study on the interface between the solid electrolyte and the conductive carbon in ASSBs.[31] In their work, Han *et al.* utilized the oxidation and reduction of LGPS as an active electrode materials by preparing the composite cathode by mixing LGPS with a large amount of carbon black.[31] While the reversible electrochemical activity of LGPS in ASSBs is interesting and rather unexpected, it strongly implies that the inclusion of carbon additives seems to stimulate the electrochemical activity of LGPS when a sufficient amount of carbon surrounds the LGPS. Furthermore, it suggests that the nature of LGPS in conventional carbon-containing composite cathodes would vary with electrochemical cycling, which has not been considered in the evaluation of the cathode performance. In this respect, here we carefully study the effect of carbon additives in ASSBs based on LGPS electrolyte. It is found that the inclusion of carbon conductive agents regardless of their physical differences such as carbon nanoparticles and carbon nanotubes in composite cathode results in the inferior performance of the cathode in comparison to that without the carbon additives. The origin of the poor performance is observed to be the large interfacial impedance which is developed during the initial cycling processes, which is related with the undesirable decomposition of the electrolyte at the interface with the carbon.

2.2 Experimental details

$Li_{10}GeP_2S_{12}$ was prepared as the previous reports described (Figure 2-1).[8] Li_2S, P_2S_5, and GeS_2 were used as starting materials. These precursors were weighed in the molar ratio of $Li_2S/P_2S_5/GeS_2 = 5/1/1$ in an argon filled glove box, sealed in a container filled with argon gas and mixed for 30 minutes using planetary ball miller (Wellcos Corporation, NBK-1, Korea). The mixed powder was pressed into pellets with 26 MPa pressure and synthesized at 550 °C for 8 hours in argon atmosphere. The sample was naturally cooled down to the ambient temperature. The composite cathode was prepared by mixing $LiNbO_3$-coated $LiCoO_2$, LGPS and conductive agents such as Super P carbon black (Hanwha Chemical, Korea), MWCNT (Hanwha

Chemical, Korea), and Denka black (Denka Company, Japan) in various weight percentage (0 wt. %, 3 wt. % and 5 wt. %). The weight ratio of LNB-LCO and LGPS was fixed to 70:30. The three components of composite cathode were hand ground by mortar and pestle for 15 minutes in order to obtain homogeneous mixture. ASSBs were assembled in a home designed cell setting (Figure 2-2). First, 70 mg of LGPS powder was filled into PEEK cell body with inner diameter of 10 mm and cold pressed with 26 MPa for 30 seconds. Then, 20 mg of prepared composite cathode was filled on one side of LGPS pellet in PEEK cell body and cold pressed with 26 MPa for 30 seconds. Thin indium foil with diameter of 9.5 mm (Alfa Aesar, 99.99%, 0.25 mm in thickness) was attached to the other side of LGPS pellet. And, lithium foil with diameter of 4 mm was placed on top of the indium foil and pressed with 4 MPa for 30 seconds. Lastly, cell casing was applied to ASSB cell in order to apply constant pressure (~15 Nm torque).

Galvanostatic cycling of the cells was carried out in voltage range of 1.9–3.6 V vs In/LiIn, which corresponds to 2.5–4.2 V vs Li^+/Li. The C-rate was calculated based on the practical capacity of $LiCoO_2$, 140 mAh g^{-1}, considering $Li_{0.5}CoO_2$ as a fully charged state. All galvanostatic tests were carried out at current rate of 0.075C and conducted using a battery test system (WBCS 3000, WonA Tech, Korea). Electrochemical Impedance Spectroscopy (EIS) was carried out after 2 cycles of ASSBs to 3.6 V vs In/LiIn at 0.075 C current rate. EIS was conducted from 3 MHz to 0.05 Hz (Model VSP-300, Bio-Logic Science Instruments, France). In the X-ray Photoelectron Spectroscopy (XPS) measurement, the pass energy was set to 23.5 eV.

In order to correct the charging effect, C 1s signal was set to 284.8 eV for ASSBs.[28] All samples were transferred under argon atmosphere with an air-tight transfer vessel. XPSPeak41 software package was used for the data analysis.

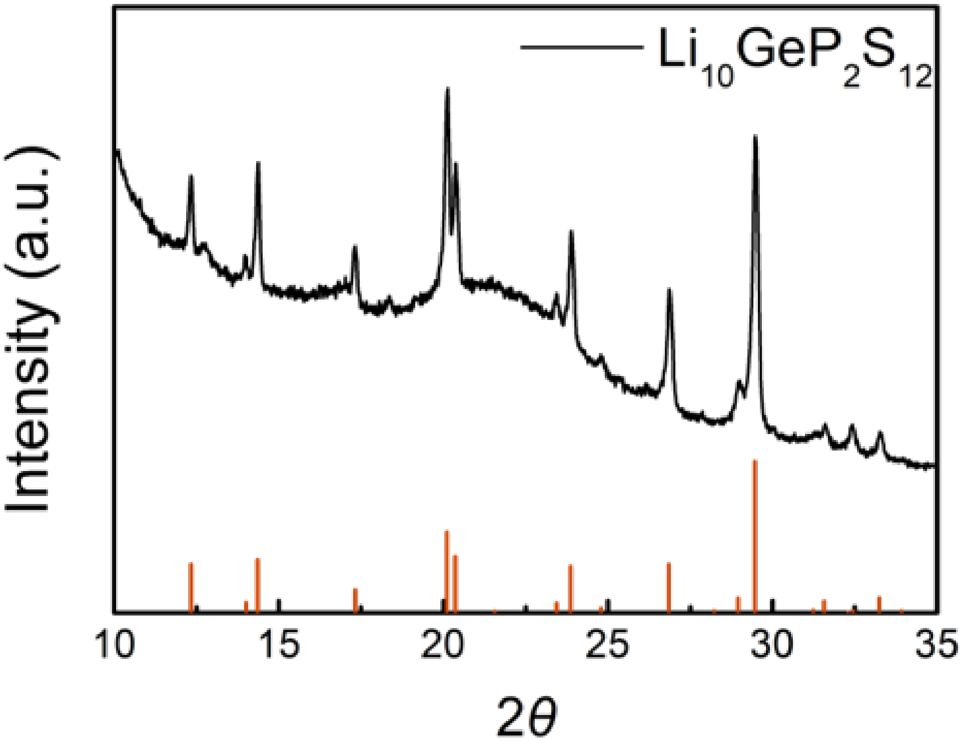

Figure 2-1. X-Ray Diffraction (XRD) pattern of LGPS solid electrolyte. XRD peaks of LGPS indicates that LGPS is successfully synthesized without side products

$Li_{10}GeP_2S_{12}$	
Temp (°C)	Conductivity (mS cm^{-1})
0	1.90
25	6.99
80	16.72

Table 2-1. Calculated ionic conductivity of LGPS. Table 2-1 shows that the ionic conductivity of LGPS in room temperature is close to the reported value in previous research.

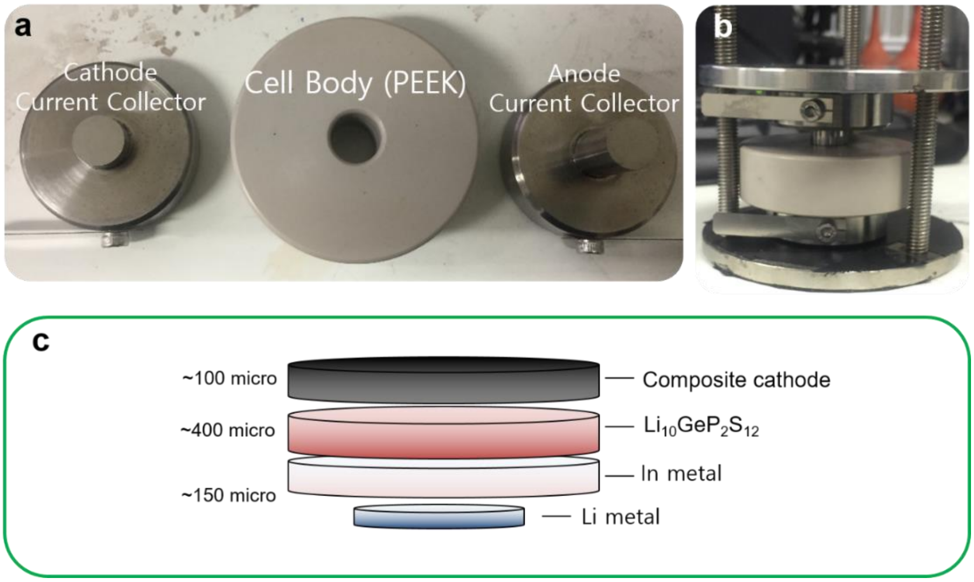

Figure 2-2. Images and schematic of ASSB employed in this work. a, Image of disassembled ASSB cell. b, Image of assembled ASSB cell with cell casing. c, Schematic of ASSB pellet inside the cell body (PEEK).

2.3 Result and discussion

2.3.1 Charge/discharge profiles of ASSBs with different types and amounts of carbon conductive agents

Charge/discharge profiles of composite cathodes comprising of $LiCoO_2$, LGPS and different ratios of carbon nanoparticles (Super P: 0, 3, and 5 wt. %) were first examined in the galvanotactic mode at 0.075C as shown in Figure 2-3a. The composite cathode without Super P carbon (red line) exhibits a typical charge/discharge profile of $LiCoO_2$ with a plateau at 3.9 V *vs.* Li/Li^+ at the given operating voltage range.[32,33] However, the inclusion of Super P in the composite results in the substantial reduction of the capacity and larger polarization between the charge and discharge despite the expectedly enhanced electrical conductivity with the added conductive agents. More careful examination of the charge profiles in Figure 2-3b reveals that there appears an unusual slope region in the beginning of the charging, which increases with the amount of the carbon added. The composite cathode with 3 wt. % Super P shows the slope region with a capacity equivalent to about 1.5 mAh g^{-1}, and that with 5 wt. % Super P exhibits a longer slope with approximately 3.5 mAh g^{-1}, which indicates that even small change in the carbon amount sensitively influences on the cathode performance. It should be noted that a similar slope region during the charging has been also observed in several previous reports adopting carbon in the ASSBs employing LGPS.[34,35] We could also confirm that such electrochemical behavior is universally observed regardless of the carbon type as shown in Figure 2-4. Employing other type of carbon nanoparticles such as Denka black or carbon nanotubes such as MWCNT consistently show the notable reduction in the capacity along with the larger polarization in comparison to the carbon-free cathode (See Figure 2-5 for the material characterization). Moreover, the cathode with MWCNT undergoes more serious degradation with a same content of carbon, which is attributed to the one-dimensional shape of MWCNT that can effectively promote the electrical network in the composite.[36-38] It hints that the undesirable side reactions that deteriorate the cathode performance are more easily triggered by the facile electrical supply in the cathode. Concerning the origin of the unusual slope from the composite cathode, it is worthwhile to note that the voltage of a pseudo-plateau in the slope begins around 2.6 V vs. Li/Li$^+$, which is similar to the voltage where LGPS oxidation occurs with a large amount of carbon (25 wt. %) as reported in a previous research.[28] It strongly suggests that the slope region in the initial charging step is a signature of the electrochemical activation and/or the subsequent degradation of LGPS, which will be discussed in more detail later.

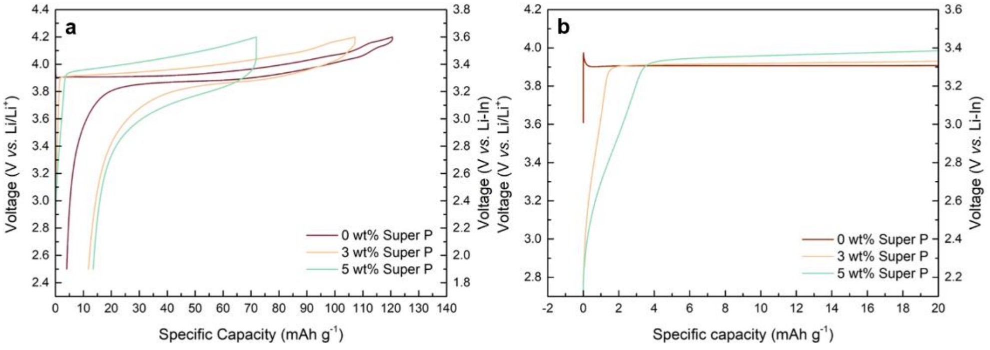

Figure 2-3. First charge/discharge profile of ASSB (Li-In/LGPS/LCO) with various wt. % of Super P (carbon additive) in composite cathode. (a) First galvanostatic discharge/charge profile of ASSB (Li-In/LGPS/LCO). (b) Magnification of first charge profile in the range of −2~20 mAh g^{-1}. All galvanostatic tests were carried out at 0.075C.

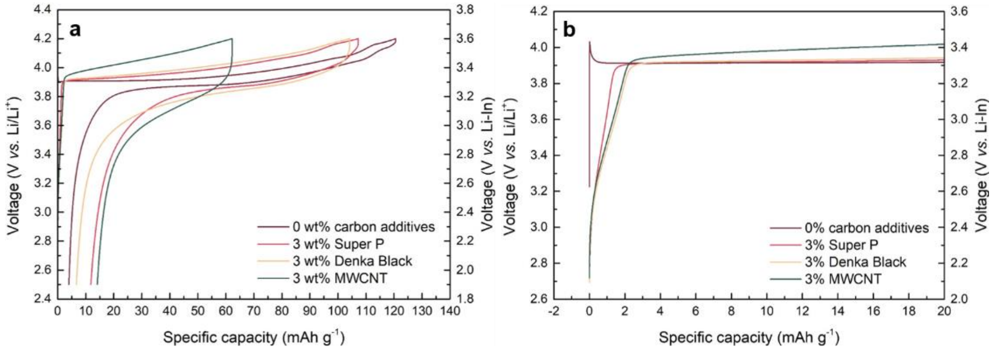

Figure 2-4. First charge/discharge profile of ASSB (Li-In/LGPS/LCO) with different types of carbon additives in composite cathode. (a) First galvanostatic discharge/charge profile of ASSB (Li-In/LGPS/LCO). (b) Magnification of first charge profile in the range of −2~20 mAh g^{-1}. All galvanostatic tests were carried out at 0.075C.

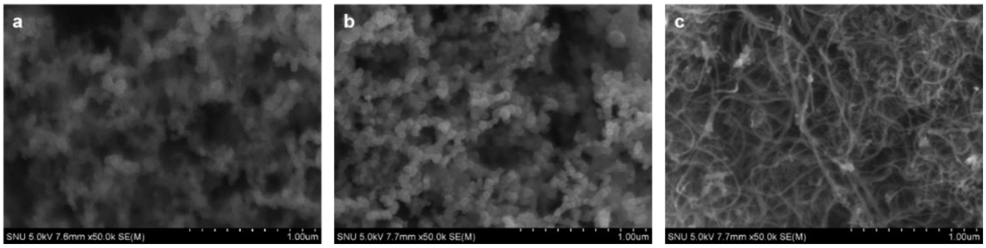

Figure 2-5. Scanning Electron Microscope (SEM) images for different types of carbon additives. a, SEM image of Super P. b, SEM image of Denka Black. c, SEM image of Multi-Walled Carbon Nanotubes (MWCNT).

2.3.2 Electrochemical Impedance Spectroscopy analysis of ASSBs with different amounts of carbon conductive agents after cycles

In order to further understand the effect of carbon additives to the electrochemical properties, EIS analysis was carried out for composite cathodes with different mass fraction of Super P after two electrochemical cycling of them. Figure 2-6a clearly shows that the impedance of the composite cathode increases with the amount of the Super P added, while the carbon-free cathode shows the lowest value. It suggests that the reduction of the capacity displayed in Figure 2-3 is primarily due to the systematic increase in the total impedance with the conductive carbon agents. In addition, the EIS analysis was further performed for the composite cathodes after extended cycle numbers (6 and 10 cycles). Figure 2-6b–d shows that the increase in the impedance is notably faster with the higher contents of carbon. While the carbon-free composite cathode exhibits negligible change in the total impedance as cycle number increases in Figure 2-6b, those with 3 and 5 wt. % Super P (Figure 2-6c and d) not only display larger total impedance but also greater increase of it with cycle, particularly during the initial a few cycles (~ 6 cycles). Our attempts to quantitatively analyze the precise factors in the impedance using several equivalent circuit models have failed due to the ambiguity in assigning interfaces such as In/LGPS, carbon/LGPS and $LiCoO_2$/LGPS.[24] Instead, concerning the speculation of the electrochemical activation and the degradation of LGPS at the interface with carbon, we compared the areas under the semi-circle at ~ 100 Hz in the EIS spectra of each samples as denoted as insets in each figure, which are typically attributed to the interfacial resistance at a cathode interface.[24] The comparison clearly reveals that the increase in the area of semi-circle for 5 wt. %-containing sample is much greater than that of the 3 wt. % one, while that of the carbon-free sample remains unchanged, supporting that the interface has been degraded with the inclusion of the carbon additives during the electrochemical cycles. Lastly, EIS analysis for ASSB with 5 wt. % Super P after various time was carried out in order to clarify whether the degradation is spontaneous or not. Figure 2-7 shows that the change in total impedance of ASSB after rest time is negligible. Furthermore, the absence of large semi-circle at ~ 100 Hz confirms that the large interfacial resistance appears from electrochemical reaction, not from chemical reaction.

Such large interfacial impedance may originate from various factors such as non-uniform current distribution and poor physical contact between electrode material and electrolyte.[13,39,40] However, since carbon additives usually offer better current distribution in a cathode matrix, it is unlikely that the presence of carbon additives would increase the total impedance of composite cathode simply by inducing non-uniform current distribution.[39] Furthermore, a significant alternation in the physical contact between electrolyte and electrode arising from the 5 wt. % carbon presence seems not plausible, especially when the ratio between LGPS and $LiCoO_2$ is fixed to 7:3, and LGPS is known to exhibit good interface contact due to their malleable property.[13]

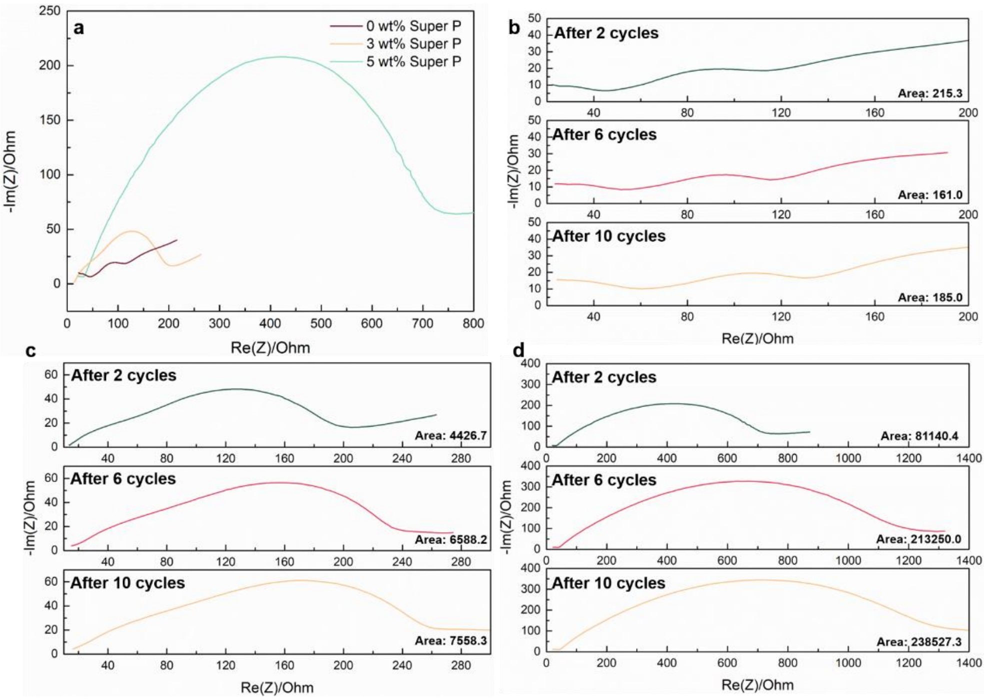

Figure 2-6. Electrochemical impedance spectrum of ASSB after 10 cycles at 0.075C with various weight ratios of Super P. (a) Electrochemical impedance spectrum of ASSB after 2 cycles at 0.075C with various weight ratios of Super P. (b) Impedance spectrum of 0 wt. % Super P after 2, 6 and 10 cycles. (c) Impedance

spectrum of 3 wt. % Super P after 2, 6 and 10 cycles. (d) Impedance spectrum of 5 wt. % Super P after 2, 6 and 10 cycles. Areas of semi-circles are calculated and displayed on the figure. All electrochemical impedance tests were performed in room temperature

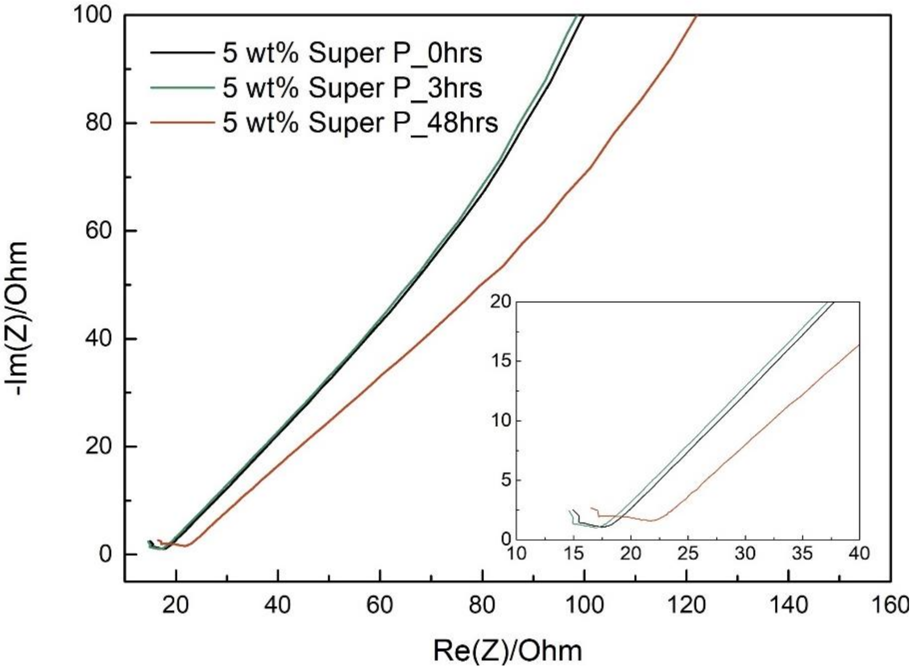

Figure 2-7. Electrochemical impedance spectra of 5 wt.% Super P containing ASSB after various rest time. The inset graph is the magnification of initial electrochemical impedance spectra of ASSB with 5 wt.% Super P.

2.3.3 X-ray Photoelectron Spectroscopy analysis of ASSBs for characterization of $Li_{10}GeP_2S_{12}$ degradation

In order to confirm the chemical change of the LGPS triggered by the presence of the carbon in the cathode interface, four samples of composite cathodes were analyzed through surface-sensitive X-ray Photoelectron Spectroscopy (XPS): carbon-free composite cathodes before and after the charge, and 5 wt. % Super P-containing composite cathodes before and after the charge, as illustrated in Figure 2-8. The fitting of the XPS spectrum of the pristine composite cathode results in roughly two main peaks at ~163 and ~161.5 eV, denoted as a high binding energy (B. E.) peak and a low B.E. peak, respectively. Although the precise designation of each peak is rather challenging due to the complicated chemical environment of S in the sample, the electronegativity difference of cations that are bonded with S could tell the general trend of the binding energy positions (S-S > P-S > Ge-S > Li-S).[31] The intensity ratio between low B.E. peak and high B.E. peak is 2.9:1 for pristine composite cathode. After the charge process, it is observed that the ratio is maintained along with the same peak positions, indicating that the electrochemical cycling does not notably degrade the LGPS in the carbon-free composite cathode. The pristine 5 wt. % carbon-containing composite cathode similarly displays two main peaks at ~163.3 and 162.1 eV with the intensity ratio of 3.1:1 comparable to that of the pristine carbon-free cathode. On the other hand, after the charge process, it notably decreases from 3.1:1 to 0.95:1 as presented in Figure 2-8b, revealing that LGPS undergoes a significant change in the structure particularly on the surface, considering the nature of the surface-sensitive XPS. Such a change with suppressed low B.E. peak and the increased high B.E. peak of sulfur suggests that the oxidation of sulfur occurred in the LGPS. Moreover, considering the fact that the low B.E peak can be primarily attributed to Li-S due to the large lithium composition in LGPS ($Li_{10}GeP_2S_{12}$), it proposes that a delithiation process has substantially taken place at the surface of LGPS with charging, which is probably followed by the formation of new S-S bonds (High B.E. peak). This speculation is consistent with the previous observation on the electrochemical reaction of LGPS as an active electrode material where lithium extraction was found to accompany with the formation of S-S bonding upon charging.[31] However, as the reversibility of the LGPS as an electrode was limited to only several cycles, its degradation is expected with the extended cycle numbers.[31] In addition, XPS spectra on C element for pristine 5 wt. % Super P composite cathode and charged 5 wt. % Super P composite cathode were compared. According to Figure 2-9, additional or disappearance of the carbon peak for pristine 5 wt. % Super P composite cathode was not observed after charge, implying that carbon act as a catalyst to promote degradation of LGPS.

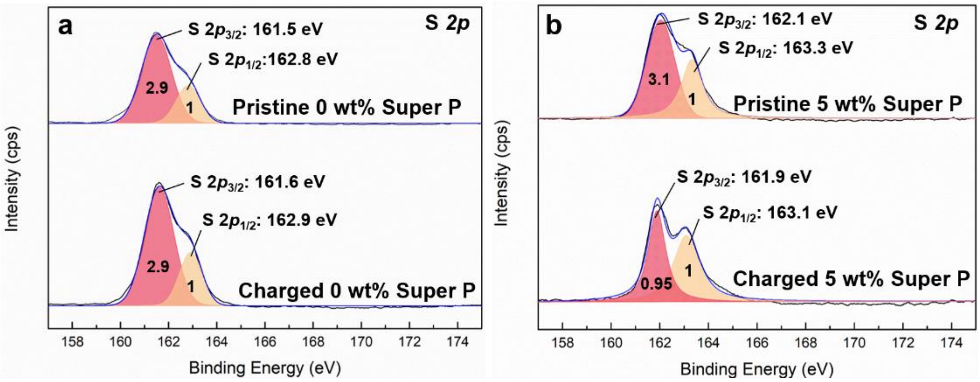

Figure 2-8. Deconvoluted S 2p XPS spectra of composite cathodes. (a) Top panel: Deconvoluted S 2p XPS spectra of pristine carbon-free composite cathode. Bottom panel: Deconvoluted S 2p XPS spectra of first charged carbon-free composite cathode. (b) Top panel: Deconvoluted S 2p XPS spectra of pristine 5 wt. % carbon-containing composite cathode. Bottom panel: Deconvoluted S 2p XPS spectra of first charged 5 wt. % carbon-containing composite cathode.

2.3.4 Impact on cycle life of ASSBs with carbon conductive agents

The participation of LGPS in the electrochemical redox reaction observed in the initial cycle also influences on the cycle life of carbon-containing composite cathodes. Figure 2-10 shows the capacity retentions of composite cathodes with 0 wt. % and 5 wt. % Super P. The carbon-free cathode maintains 85% of the theoretical capacity of $LiCoO_2$ after 35 cycles under the current rate of 0.075C. On the other hand, the carbon-containing cathode exhibits substantially low capacity along with the coulombic efficiency that far deviates from 100%, delivering 43% of theoretical capacity of $LiCoO_2$ throughout 35 cycles. The slight fluctuation of the discharge capacity throughout 35 cycles is attributed to the decomposition products of LGPS that destabilizes the transport of ions at the interface. The formation and accumulation of side products from LGPS at the interface are expected to hinder Li^+ transfer, which would increase the impedance of the cell. Furthermore, compared with the pristine LGPS, side products from the decomposition may have different mechanical properties such as ductility.[13] The transformed physical property may not be ductile enough to withstand the stress applied to the cell. While the overall discharge capacity is substantially low, the relative cycle degradation is not as severe as expected. It is speculated that the degradation of LGPS mainly takes place at the initial cycle near the carbon hampering the ionic transport, however, it does not propagate to further influence on the transport, and the degradation of LGPS, and the degradation of LGPS that is originally far from the carbon remains limited due to the lack of electrical contact. The disappearance of the additional slope after the second cycle also supports that the major decomposition of LGPS occurs at the first charging step (Figure 2-11).

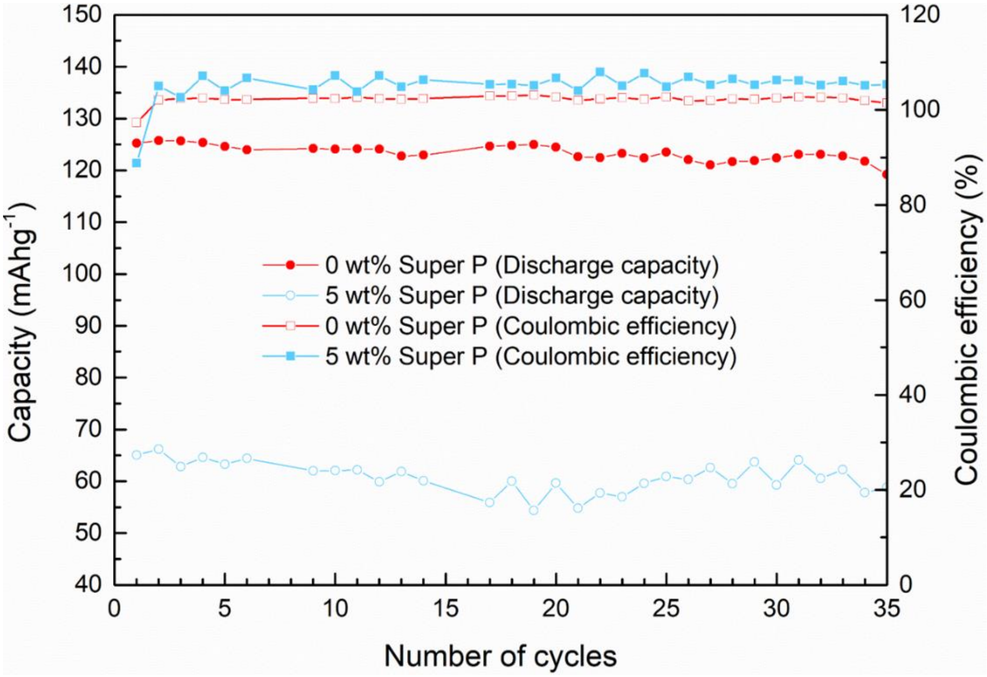

Figure 2-10. Cycle performance of all-solid-state battery with/without carbon additives in composite cathode. The ASSB with carbon additive (Super P) shows not only decreased initial discharge capacity but also unstable cycle life of ASSB compared to carbon-free ASSB. While capacity of carbon-free ASSB is steadily maintained about 125 mAh g^{-1}, capacity of 5 wt. % Super P-containing ASSB is unstable throughout 35 cycles

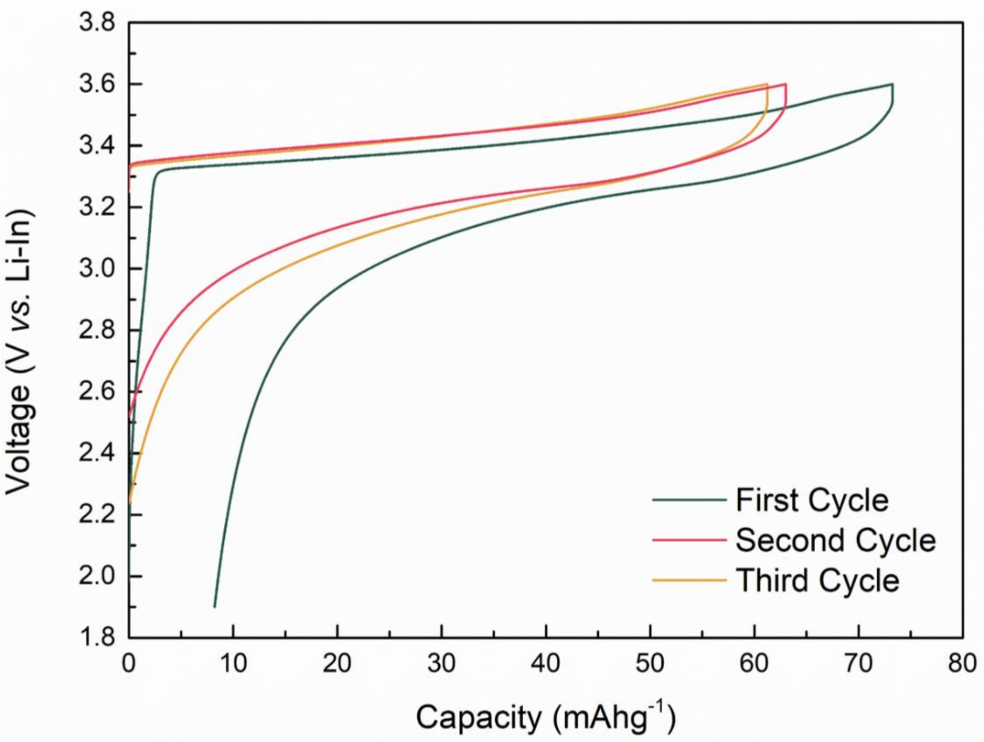

Figure 2-11. Electrochemical profile of 5 wt. % Super P-containing ASSB.

Electrochemical profile of 5 wt. % Super P-containing ASSB for initial three cycles is shown. The additional slope in charging step is only observed in first charging process.

2.4 Concluding remarks

Introduction of carbon additives in composite cathode induces a large polarization during charging and discharging, followed by the decreased initial capacity along with an unusual voltage slope at around 2.6 V vs Li/Li$^+$. The degradation of the electrochemical performance of the carbon-containing cathode composite is found to be correlated with the severe impedance increase at the cathode interface during cycles. The surface analysis of the composite cathode with carbon added revealed that the oxidation of sulfur occurs in LGPS during charging, involving the loss of the substantial lithium and the formation of sulfur-sulfur bonding, which is indicative of the degradation of LGPS. It is believed that the deterioration of the LGPS with carbon that triggers the electrochemical reaction of LGPS increases the interfacial impedance in the composite cathode by interfering the Li$^+$ pathway. Moreover, such Li$^+$ pathway interference induces large polarization and serious capacity loss in ASSBs. This work shows that carbon additives which are crucial for constructing high power density ASSBs, can undermine the electrochemical performance of ASSB employing sulfide electrolytes. As we face a dilemma in constructing ASSB concerning the conductive agent, which provides the electronic pathway but simultaneously promotes the degradation of the electrolyte, optimally balancing them or finding a suitable conductive agent with a minimal influence on the electrolyte is essential in designing high power density ASSBs employing sulfide electrolytes.

2.5 References

1. Molina, B. This again: lithium-ion batteries behind HP recall. *USA Today* https://www.usatoday.com/story/tech/news/2017/01/25/hp-expands-recall-laptop-batteries/97042680/ (2017).
2. Warren, T. HP recalls 101,000 laptop batteries over fire concerns. *The Verge* https://www.theverge.com/2017/1/25/14384052/hp-laptop-battery-recall-2017 (2017).
3. Hess, S., Wohlfahrt-Mehrens, M. & Wachtler, M. Flammability of Li-Ion Battery Electrolytes: Flash Point and Self-Extinguishing Time Measurements. *J. Electrochem. Soc.* **162**, A3084-A3097 (2015).
4. Kerman, K., Luntz, A., Viswanathan, V., Chiang, Y.-M. & Chen, Z. Review—Practical Challenges Hindering the Development of Solid State Li Ion Batteries. *J. Electrochem. Soc.* **164**, A1731-A1744 (2017).
5. Xiayin, Y. *et al.* All-solid-state lithium batteries with inorganic solid electrolytes: Review of fundamental science. *Chin. Phys. B* **25**, 018802 (2016).
6. Kim, J.-J., Yoon, K., Park, I. & Kang, K. Progress in the Development of Sodium-Ion Solid Electrolytes. *Small Methods* **1**, 1700219-n/a (2017).

7. Han, X. *et al.* Negating interfacial impedance in garnet-based solid-state Li metal batteries. *Nat. Mater.* **16**, 572 (2016).

8. Kamaya, N. *et al.* A lithium superionic conductor. *Nat. Mater.* **10**, 682 (2011).

9. Kim, D. H. *et al.* Infiltration of Solution-Processable Solid Electrolytes into Conventional Li-Ion-Battery Electrodes for All-Solid-State Li-Ion Batteries. *Nano Lett.* **17**, 3013-3020 (2017).

10. Liu, Z. *et al.* Anomalous High Ionic Conductivity of Nanoporous β-Li_3PS_4. *J. Am. Chem. Soc.* **135**, 975-978 (2013).

11. Minami, K., Hayashi, A. & Tatsumisago, M. Crystallization Process for Superionic $Li_7P_3S_{11}$ Glass–Ceramic Electrolytes. *J. Am. Ceram. Soc.* **94**, 1779-1783 (2011).

12. Hayashi, A., Hama, S., Morimoto, H., Tatsumisago, M. & Minami, T. Preparation of Li_2S–P_2S_5 Amorphous Solid Electrolytes by Mechanical Milling. *J. Am. Ceram. Soc.* **84**, 477-479 (2001).

13. Sakuda, A., Hayashi, A. & Tatsumisago, M. Sulfide Solid Electrolyte with Favorable Mechanical Property for All-Solid-State Lithium Battery. *Sci. Rep.* **3**, 2261 (2013).

14. Ohta, S. *et al.* All-solid-state lithium ion battery using garnet-type oxide and Li_3BO_3 solid electrolytes fabricated by screen-printing. *J. Power Sources* **238**, 53-56 (2013).

15. Ohta, S., Kobayashi, T., Seki, J. & Asaoka, T. Electrochemical performance of an all-solid-state lithium ion battery with garnet-type oxide electrolyte. *J. Power Sources* **202**, 332-335 (2012).

16. Kotobuki, M., Kanamura, K., Sato, Y. & Yoshida, T. Fabrication of all-solid-state lithium battery with lithium metal anode using Al_2O_3-added $Li_7La_3Zr_2O_{12}$ solid electrolyte. *J. Power Sources* **196**, 7750-7754 (2011).

17. Fu, K. *et al.* Three-dimensional bilayer garnet solid electrolyte based high energy density lithium metal-sulfur batteries. *Energy Environ. Sci.* **10**, 1568-1575 (2017).

18. Du, F. *et al.* All solid state lithium batteries based on lamellar garnet-type ceramic electrolytes. *J. Power Sources* **300**, 24-28 (2015).

19. Xu, B., Duan, H., Liu, H., Wang, C. A. & Zhong, S. Stabilization of Garnet/Liquid Electrolyte Interface Using Superbase Additives for Hybrid Li Batteries. *ACS Appl. Mater. Interfaces* **9**, 21077-21082 (2017).

20. Wenzel, S. *et al.* Direct Observation of the Interfacial Instability of the Fast Ionic Conductor $Li_{10}GeP_2S_{12}$ at the Lithium Metal Anode. *Chem. Mater.* **28**, 2400-2407 (2016).

21. Sakuda, A., Hayashi, A. & Tatsumisago, M. Interfacial Observation between $LiCoO_2$ Electrode and $Li_2S-P_2S_5$ Solid Electrolytes of All-Solid-State

Lithium Secondary Batteries Using Transmission Electron Microscopy. *Chem. Mater.* **22**, 949-956 (2010).

22. Wenzel, S. *et al.* Interphase formation and degradation of charge transfer kinetics between a lithium metal anode and highly crystalline $Li_7P_3S_{11}$ solid electrolyte. *Solid State Ionics* **286**, 24-33 (2016).

23. Kobayashi, Y. *et al.* 5 V Class All-Solid-State Composite Lithium Battery with Li_3PO_4 Coated $LiNi_{0.5}Mn_{1.5}O_4$. *J. Electrochem. Soc.* **150**, A1577-A1582 (2003).

24. Ohta, N. *et al.* $LiNbO_3$-coated $LiCoO_2$ as cathode material for all solid-state lithium secondary batteries. *Electrochem. Commun.* **9**, 1486-1490 (2007).

25. Sakuda, A., Kitaura, H., Hayashi, A., Tadanaga, K. & Tatsumisago, M. Improvement of High-Rate Performance of All-Solid-State Lithium Secondary Batteries Using $LiCoO_2$ Coated with Li_2O-SiO_2 Glasses. *Electrochem. Solid State Lett.* **11**, A1-A3 (2008).

26. Sakuda, A., Hayashi, A. & Tatsumisago, M. Electrochemical performance of all-solid-state lithium secondary batteries improved by the coating of $Li_2O–TiO_2$ films on $LiCoO_2$ electrode. *J. Power Sources* **195**, 599-603 (2010).

27. Seino, Y., Ota, T. & Takada, K. High rate capabilities of all-solid-state lithium secondary batteries using $Li_4Ti_5O_{12}$-coated $LiNi_{0.8}Co_{0.15}Al_{0.05}O_2$ and a sulfide-based solid electrolyte. *J. Power Sources* **196**, 6488-6492 (2011).

28. Visbal, H. *et al.* The effect of diamond-like carbon coating on $LiNi_{0.8}Co_{0.15}Al_{0.05}O_2$ particles for all solid-state lithium-ion batteries based on $Li_2S–P_2S_5$ glass-ceramics. *J. Power Sources* **314**, 85-92 (2016).

29. Li, W. J., Hirayama, M., Suzuki, K. & Kanno, R. Fabrication and electrochemical properties of a $LiCoO_2$ and $Li_{10}GeP_2S_{12}$ composite electrode for use in all-solid-state batteries. *Solid State Ionics* **285**, 136-142 (2016).

30. Menetrier, M., Saadoune, I., Levasseur, S. & Delmas, C. The insulator-metal transition upon lithium deintercalation from $LiCoO_2$: electronic properties and 7Li NMR study. *J. Mater. Chem.* **9**, 1135-1140 (1999)

31. Han, F., Gao, T., Zhu, Y., Gaskell, K. J. & Wang, C. A Battery Made from a Single Material. *Adv. Mater.* **27**, 3473-3483 (2015).

32. Mizushima, K., Jones, P. C., Wiseman, P. J. & Goodenough, J. B. Li_xCoO_2 (0<x<-1): A new cathode material for batteries of high energy density. *Mater. Res. Bull.* **15**, 783-789 (1980).

33. Cho, J., Kim, Y. J. & Park, B. Novel $LiCoO_2$ Cathode Material with Al_2O_3 Coating for a Li Ion Cell. *Chem. Mater.* **12**, 3788-3791 (2000)

34. Oh, G., Hirayama, M., Kwon, O., Suzuki, K. & Kanno, R. Bulk-Type All Solid-State Batteries with 5 V Class $LiNi_{0.5}Mn_{1.5}O_4$ Cathode and $Li_{10}GeP_2S_{12}$ Solid Electrolyte. *Chem. Mater.* **28**, 2634-2640 (2016).

35. Tatsumisago, M., Mizuno, F. & Hayashi, A. All-solid-state lithium secondary batteries using sulfide-based glass–ceramic electrolytes. *J. Power Sources* **159**, 193-199 (2006).

36. Peng, H.-J. *et al.* Nanoarchitectured Graphene/CNT@Porous Carbon with Extraordinary Electrical Conductivity and Interconnected Micro/Mesopores for Lithium-Sulfur Batteries. *Adv. Funct. Mater.* **24**, 2772-2781 (2014).

37. Wei, W. *et al.* CNT enhanced sulfur composite cathode material for high rate lithium battery. *Electrochem. Commun.* **13**, 399-402 (2011).

38. Ahn, W., Kim, K.-B., Jung, K.-N., Shin, K.-H. & Jin, C.-S. Synthesis and electrochemical properties of a sulfur-multi walled carbon nanotubes composite as a cathode material for lithium sulfur batteries. *J. Power Sources* **202**, 394-399 (2012).

39. Dominko, R. *et al.* The role of carbon black distribution in cathodes for Li ion batteries. *J. Power Sources* **119-121**, 770-773 (2003).

40. Auvergniot, J. *et al.* Interface Stability of Argyrodite Li_6PS_5Cl toward $LiCoO_2$, $LiNi_{1/3}Co_{1/3}Mn_{1/3}O_2$, and $LiMn_2O_4$ in Bulk All-Solid-State Batteries. *Chem. Mater.* **29**, 3883-3890 (2017).

Chapter 3. Detrimental effect of high-temperature storage on sulfide-based all-solid-state batteries

(The content of this chapter has been published in *Appl. Phys. Rev.* [Yoon, K., Kim, H. *et al., Appl. Phys. Rev.* **2022**, 9, 031403.]-Reproduced by permission of AIP Publishing Group)

3.1 Introduction

As the application of the modern battery system has extended from small electronic devices such as cell phones to electric vehicles (EVs), finding safer and more energy-dense batteries has become a central mission.[1–5] While the lithium-ion battery (LIB) has been the most widely adopted, its employment in new large-scale applications brings about concerns on the safety risk that scales with the size of batteries. Fabrication defects or the misuse of LIBs can cause catastrophic thermal runaway reactions involving the combustion of constituting organic liquid electrolytes, thereby leading to battery explosion.[6–10] In fact, a few recent safety incidents of EVs were found to be related to the instability/malfunction of LIBs, which underscores the need for safer alternative batteries.[11] Today, all-solid-state batteries (ASSBs) employing non-flammable solid electrolytes are considered as one of the most promising candidates for EVs with respect to the safety.[12–16] Moreover, the rapid development of high-energy-density ASSBs in recent years through extensive research efforts—by leveraging the high-capacity lithium metal and the versatile form factor—further expedites the potential implementation of ASSB in large-scale EVs.[4,13,17–21]

When considering batteries for EVs, one of the notable aspects that differ from the use in small electronic devices is their distinct operation conditions. Batteries in typical electronic devices such as cell phones undergo relatively moderate temperature variation and only experience constant modes of either charge or discharge. On the other hand, batteries employed in EVs are expected to be exposed to a wider temperature variation due to their outdoor storage. Moreover, the intermittent usage/parking of these vehicles keeps the batteries at rest in charged states for most of the time without being used. It implies that calendar aging properties of batteries at different states of charges (SOC) would be one of the most decisive factors in securing the reliability of battery systems in EVs under varying outdoor environments. Nevertheless, it is still elusive, to the best of our knowledge, how the storage capability of ASSBs would be affected by hot or cold weather for a practically long time with regard to their SOCs, although ASSBs are emphasized as the imminent alternative system for EV applications.[22–25]

In this work, we investigate the calendar aging properties of the most representative ASSB system comprising of Li_6PS_5Cl solid electrolyte and commercial $LiNi_{0.8}Co_{0.1}Mn_{0.1}O_2$ (NCM811) cathode, mimicking the practical storage conditions of EVs in varying outdoor conditions.[26] It is carefully examined how the performance of ASSB is retained/altered when exposed to (i) outdoor temperatures (e.g., 20, 20, and 70 °C), (ii) for an extended rest period (up to a maximum of six days), and (iii) at a charged state (4.3 V), in comparison with the conventional LIBs. Our results reveal that the Li_6PS_5Cl–NCM811 ASSB can retain its performance remarkably well at low temperatures, which excels the calendar aging properties of equivalent lithium cells containing liquid electrolyte. On the other hand, a substantial deterioration of ASSB is observed after the storage at high temperature, which is accompanied by a significant increase in the overpotential and the decrease in the capacity to almost less than a half of the deliverable capacity, making a clear contrast to the reference lithium cells employing the liquid electrolyte. From the extensive characterizations, we reveal that this degradation is correlated with the corrosion of the cathode/electrolyte interface, developing a detrimental porous interface structure that results in the physical particle-to-particle disconnect. We propose that the thermal instability of the partially delithiated Li_6PS_5Cl at this temperature promotes the side reactions with the NCM811 cathode material involving gaseous by-products such as SO_x gas, which rapidly deteriorates the interface between the cathode and the Li_6PS_5Cl. While several previous studies reported the high temperature instability of ASSBs with respect to the cathode/electrolyte interface arising from the interdiffusion decomposition such as in $LiNi_{1/3}Co_{1/3}Mn_{1/3}O_2$ and $75Li_2S$-$25P_2S_5$ glass systems,[27] our key message here is that the delithiated Li_6PS_5Cl electrolyte itself can decompose into LiCl, amorphous sulfide glasses, and SO_x gas after several days of storage at as low as 70 °C. This is a new degradation phenomenon that cannot be prevented by simple surface coating or interface protection and has not been reported before.

3.2 Experimental details

3.2.1 Synthesis of $LiNbO_3$-coated NCM811

Commercial NCM811 (Toshima Manufacuring Co.) with particle size of about 10 μm was first placed in anhydrous ethanol (Sigma-Aldrich, anhydrous ≥99.5%), and lithium ethoxide (Sigma-Aldrich, 1.0 M in ethanol) and niobium(V) ethoxide (Sigma-Aldrich, 99.95%) were added in mole ratio to synthesize 1.5 wt. % of $LiNbO_3$. The solution was stirred and dried at 300 RPM and 70 °C until the solvent was completely dried. Finally, the dried samples were sintered at 400 °C for 2 hours under the flowing O_2 atmosphere in a tube furnace to finally obtain 1.5 wt. % of $LiNbO_3$-coated NCM811.

3.2.2 Cell assembly of solid-state cells

NCM811 composite cathode/Li_6PS_5Cl/Li-In cells were assembled with homemade pressurized cell as demonstrated in a previous report[16]. Argyrodite sulfide solid electrolyte, Li_6PS_5Cl (Jeong Kwan corp.) exhibits ionic conductivity of 1.5×10^{-3} S cm^{-1} at room temperature and powder size of about 1 μm. NCM811 composite cathodes are comprised of $LiNbO_3$ coated cathode material (NCM811), solid electrolyte (Li_6PS_5Cl), and conducting carbon additives (Super P) in weight ratio of 70:30:3. The composite cathodes were prepared by dry-mixing using mortar and pestle for 30 minutes. Anodes, Li-In alloy electrodes, were manufactured in nominal composition of $Li_{0.5}In$. The $Li_{0.5}In$ was prepared by mixing Li powder (FMC Lithium corp.) and In powder (Sigma-Aldrich, 99.99%) for 30 minutes by vortex mixer

(Scientific Industries, Inc). Li_6PS_5Cl-carbon composite cathodes were prepared by mixing Li_6PS_5Cl and Super P carbon in ratio of 10:1. The composite cathodes were prepared by dry-mixing using mortar and pestle for 30 minutes. ASSB cells with a diameter of 10 mm, composed of SUS rods as the current collectors and polyaryletheretherketone (PEEK) mold, were assembled as shown in previous report[16].

3.2.3 Cell assembly of liquid electrolyte cells

The cathode slurry composed of 92 wt. % NCM811, 4 wt. % carbon black (Super P, Timcal, Switzerland), and 4 wt. % polyvinylidene fluoride (PVDF, Sigma Aldrich) binder, dissolved in N-methyl1,2-pyrrolidone (NMP; Sigma-Aldrich, USA), was cast onto Al foil, and dried in a 70 °C vacuum oven overnight to evaporate NMP. Coin cells (CR2032, Hohsen) were assembled using the electrodes, a lithium counter electrode, a separator (GF/F filter, Whatman) and a 1 M solution of $LiPF_6$ in a mixture of ethyl carbonate and dimethyl carbonate (EC/DMC, 1/1 v./v.) in an Ar-filled glove box.

3.2.4 Electrochemical measurements

Electrochemical experiments were performed using a potentiogalvanostat (WBCS 3000, WonA Tech, Korea). NCM811 solid-state and liquid electrolyte cells were charged to 4.3 V *vs.* Li/Li^+ with 0.1 C rate and stored for six days under three different temperatures of -20 °C, 20 °C and 70 °C. The 4.3 V charged NCM811 ASSBs were stored at an inert environment (vacuum or Ar). After 6 days of storage, subsequent discharge/charge (0.1 C rate) protocol was conducted at room temperature to evaluate cycle performance in the operation voltage of 3.0 – 4.3 V *vs.* Li/Li^+ at 0.1 C rate. EIS measurements were performed for the cells after the -20 °C, 20 °C and 70 °C-stored cells to investigate the changes in the impedance. Bio-Logic (VMP3) was used for the EIS measurements from 3 MHz to 0.1 Hz with an amplitude of 10 mV.

3.2.5 Detailed information on electrochemical protocol

All solid-state cells undergo charge/discharge initial cycle in voltage range of 3.0 – 4.3 V vs. Li/Li^+ at 0.1 C rate under operation temperature of 25 °C. After initial cycle, all solid-state cells are charged up to 4.3 V at 0.1 C rate under operation temperature of of 25 °C as shown in Figure 3-1 and stored at three different temperatures: -20, 20 and 70 °C. All samples are stored under inert environment (Ar/vacuum) for six days. After storages of solid-state cells, all stored solid-state cells are rested under 25 °C inert environment for six hours and subsequent discharge protocol is carried on at 0.1 C rate.

3.2.6 X-ray diffraction

For the 4.3 V charged NCM811 solid-state cells stored in three different temperatures, XRD (D8 ADVANCE, Bruker and D2 PHASER, Bruker) analysis was conducted with Cu-Kα radiation (λ=1.54178Å) at a scanning speed of 0.01° min^{-1} in the 2θ range of 10–75°. NCM811 solid-state electrolyte cells were charged to 4.3 V *vs.* Li/Li^+ with 0.1 C rate and stored for six days under three different temperatures of -20 °C, 20 °C and 70 °C. After the storage at respective temperature, the cathode composite containing NCM811 and the solid electrolyte was retrieved by dissembling the cell in the Ar-filled glovebox. Subsequently, the 4.3 V charged NCM811 cathode composite was analyzed by XRD in the 2θ range of 10–75°. Rietveld refinement of the XRD patterns was performed using the FullProf program[52] as shown in Figure 3-2.

3.2.7 Tender XAS

Tender XAS spectra of 4.3 V solid-state cells stored in three different temperatures, were obtained at beamline 1C of the Pohang Light Source-II and BL16A1 beamline of the National Synchrotron Radiation Research Center (NSRRC) in Taiwan. Spectra were collected in bulk sensitive fluorescence yield mode at an energy step of 0.1eV in the range of 2140–2180eV (P K edge), 2460–2490eV (S K edge), 2820–2860eV (Cl K edge). Background subtraction and normalization were performed by using the Athena software.

3.2.8 Scanning electron microscopy

Field-emission scanning electron microscopy (SU-70, Hitachi) analysis was utilized to observe the surface morphological changes of 4.3 V charged NCM811 composite cathode after the six days of storage at three different temperatures.

3.2.9 STA-MS

Simultaneous thermal analyzer-mass spectrometer (STA 409 PC + QMS 403 C, NETZSCH) was employed to observe mass change and gas evolution from 4.3 V charged NCM811 composite cathode. Measurements were carried out in Ar atmosphere. The sample mass was 25 mg. Samples were heated from 33 °C to 100 °C with a heating rate of 1 °C /min.

3.2.10 Detailed explanation on change in Li diffusion coefficients after the different storage conditions.

Li diffusion coefficient is related to Warburg impedance as the following equation, where D_{Li^+} is the Li^+ diffusion coefficient, R is the gas constant, T is the absolute temperature, A is the interfacial area between the electrode and electrolyte, n is the number of electrons per molecule oxidized, F is the Faraday constant, C is the concentration, and A_w is the Warburg factor.[1]

$$D_{Li^+} = R^2T^2/2A^2n^4F^4C^2A_w^2$$

Since it is technically infeasible to determine the accurate interfacial area between NCM811 and Li_6PS_5Cl in the composite cathode (i) due to the nature of the solid-solid contact and (ii) the observed evolution of the gas evolution at the interface upon the storage at the elevated temperature, we have obtained D_{Li^+} value in terms of A, assuming n and C values are equal to 1. Figure 3-3 presents that the D_{Li^+} value of composite cathode stored under 70 °C exhibits approximately 100-fold smaller value compared with those stored under -20 and 20 °C. This area-normalized D_{Li^+} clearly supports that the active interfacial area between NCM811 and Li_6PS_5Cl in the composite cathode has been significantly reduced with the 70 °C-storage and is compatible with the proposed morphology.

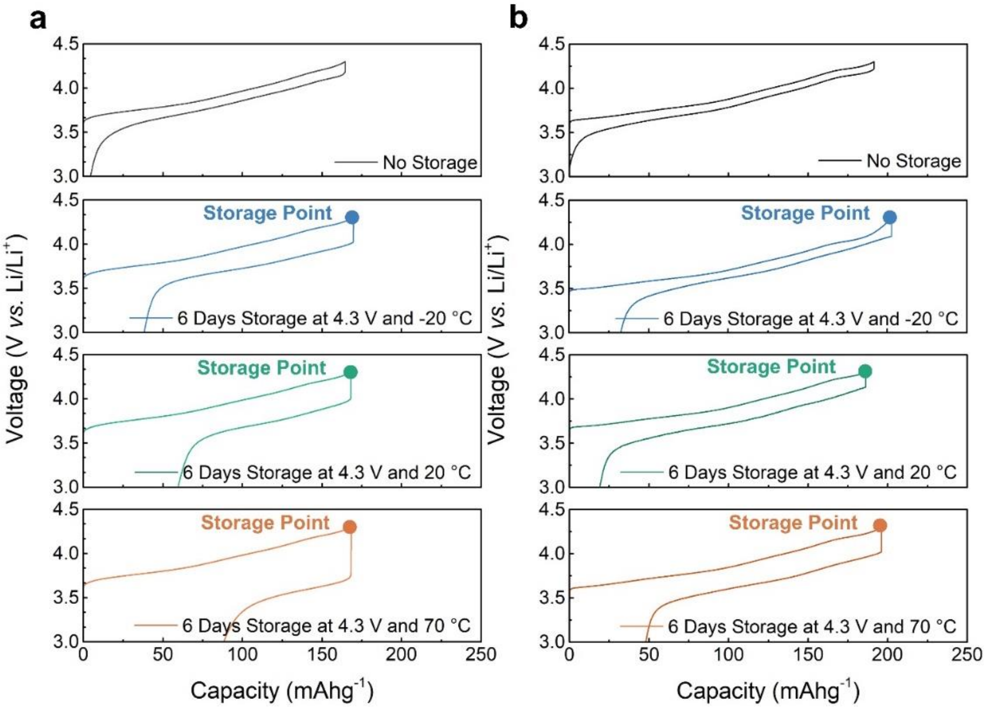

Figure 3-1. Voltage profiles of solid-state cells and liquid electrolyte cells employing NCM811 at various storage temperatures. a) Second charge curves of solid-state cells before storage conditions and subsequent discharge curves after three different storage temperatures. b) Second charge curves of liquid electrolyte cells before storage conditions and subsequent discharge curves after three different storage temperatures.

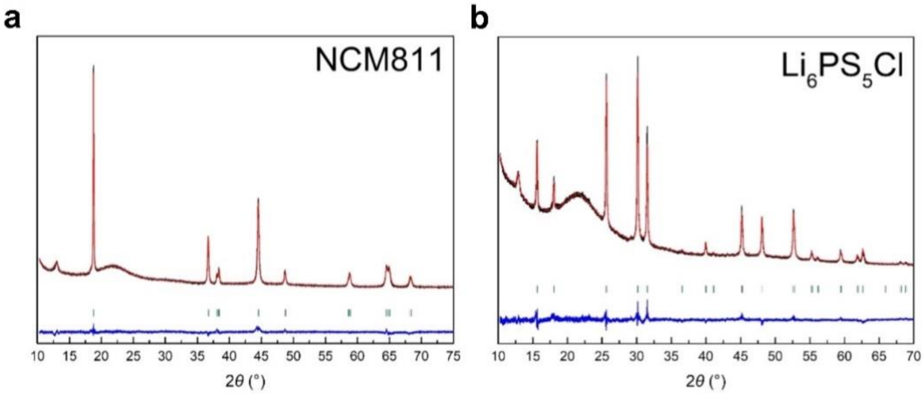

Figure 3-2. X-ray diffraction and Rietveld refinement of NCM811 and Li_6PS_5Cl. a) Rietveld refinement plot showing the observed (black) and calculated (red) diffraction data and their difference (blue) for NCM811. b) Rietveld refinement plot showing the observed (black) and calculated (red) diffraction data and their difference (blue) for Li_6PS_5Cl.

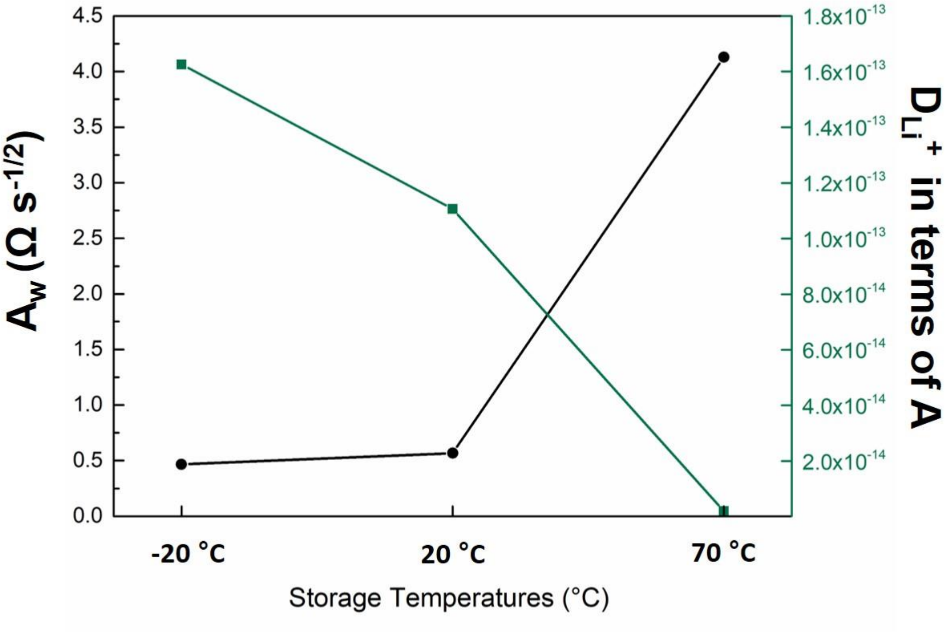

Figure 3-3. Warburg factor and Li diffusion coefficient. D_{Li+} value is plotted in terms of A, assuming n and C values are equal to 1 for simple calculation.

3.3 Result and discussion

3.3.1 Electrochemical performances of solid-state and liquid electrolyte cells after various storage temperatures

NCM811 polycrystalline particles with an average size of 10 μm were chosen as a model cathode active material in the Li_6PS_5Cl-based ASSB system (Figure 3-4). $LiNbO_3$ nanoparticles (1.5 wt. %) were coated on the surface of NCM811 particles (LNbO–NCM811) for the interface compatibility between NCM811 and Li_6PS_5Cl, which has been proven to be effective in preventing the potential interfacial side reactions according to previous literature.[28,29] For the storage experiments, the solid-state lithium cell comprising of LNbO–NCM811 and Li_6PS_5Cl was first charged to 4.3 V (vs Li/Li^+) at a current rate of 0.1 C after the initial cycle and stored in three different conditions of –20, 20, and 70 °C for six days. Figure 3-5a displays charge/discharge profiles of the solid-state cells after the storage at these three conditions, which have been all measured at room temperature in the same condition for comparisons [refer to Figure 3-1a and 3.2.5 Detailed information on electrochemical protocol]. It illustrates that typical electrochemical profiles of NCM811 are observable for the cells after the six-day storage at –20 and 20 °C, which also depicts no significant difference compared with the reference cell that has not undergone the storage experiment (top panel). Not only the specific capacities but also the voltage hysteresis remained nearly unchanged even after almost a week of storage. This is a rather remarkable calendar aging performance, since it is widely known that the prolonged storage of conventional LIBs at charged states is prone to exhibiting a noticeable increase in the cell resistance.[30–32] In this respect, we constructed similar electrochemical cells of the LNbO–NCM811 cathode employing the conventional liquid electrolyte and conducted the same storage experiments as depicted in Figure 3-1b and Figure 3-5b. It shows that the six-day storage at –20 or 20 °C leads to a relatively larger voltage hysteresis than that was observed in the cell without the storage, which is consistent with the previous literature.[30,33,34] Considering that the gradual increase in the cell resistance over time has been generally attributed to the accumulation of passivating byproducts on the active materials from the side reactions between electrolyte and electrode,[30,35,36] it suggests the relative stability of the interface in the solid-state lithium cells at ambient or low temperature even for an extended storage time.

On the other hand, we found that the storage at a higher temperature (70 °C) leads to a drastic performance degradation of the solid-state lithium cell at room temperature, as presented in the bottom panel of Figure 3-5a. It depicts that the discharge capacity after the storage decreases to less than a half of the initial deliverable capacity. Moreover, the voltage hysteresis between the charge and discharge became markedly greater than what were observed for cases of the storage at low temperatures. Notably, it also contrasts to the case of the reference cell employing the liquid electrolyte at the same storage conditions in Figure 3-5b. Even though a slight increase in the voltage hysteresis was observed for the reference cells after the storage, it did not show noticeable difference in the degree of degradation regardless of the storage temperature (e.g., –20, 20, and 70 °C) unlike the solid-state lithium cells. The performance degradation of the solid-state cell after the 70 °C storage was also observed consistently during the subsequent cycles, as depicted in Figure 3-5c. The cycle data show that the loss of the deliverable capacity could not be recovered with repeated charge and discharge processes at room temperature, indicating that it is likely due to the permanent damage of the cell, not to the temporary phenomena such as the self-discharge after the storage.[37] On the contrary, all other cells either employing solid (after –20 and 20 °C storage) or liquid electrolyte could stably retain the original capacity over the cycles, as shown in Figure 3-5d.

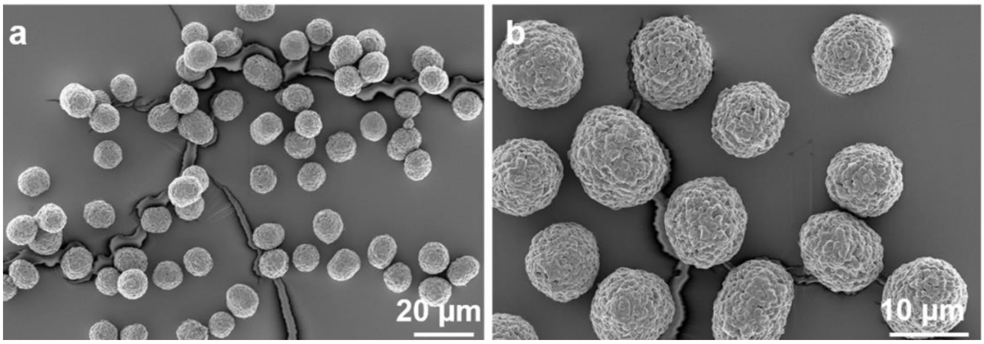

Figure 3-4. SEM images of NCM811 cathode active materials. a) low magnification SEM image of NCM811. b) high magnification SEM image of NCM811.

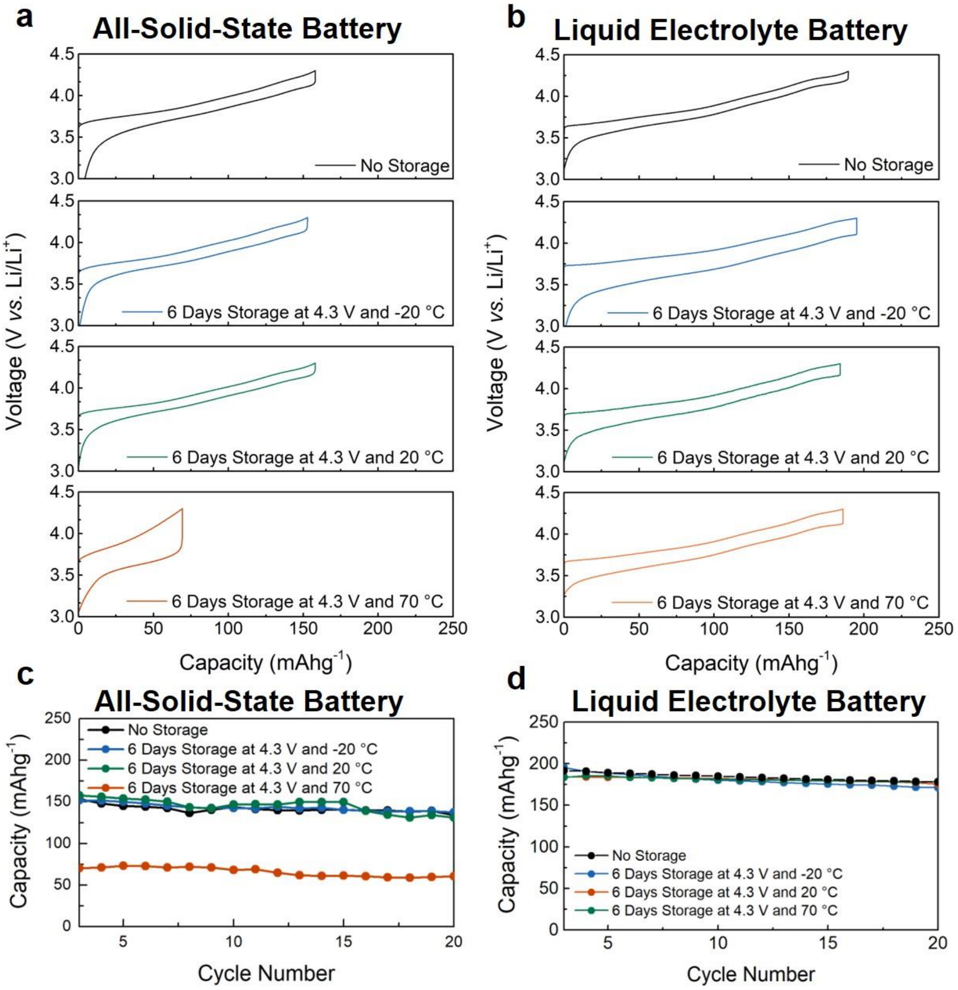

Figure 3-5. Voltage profiles and cycle life of solid-state cells and liquid electrolyte cells employing NCM811 after exposure to various storage temperatures. (a) Third charge/discharge curves of all-solid-state batteries after four different storage conditions: no storage, six days of storage at −20, 20, and 70 °C. (b) Third charge/discharge curves of liquid electrolyte batteries after four different storage conditions: no storage, 4.3 V charged solid-state cells from six days of storage at −20, 20, and 70 °C. (c) Cycle life of solid-state cells after exposure to four

different storage conditions. (d) Cycle life of liquid electrolyte cells after exposure to four different storage conditions.

3.3.2 Redox activities of solid-state and liquid electrolyte cells after various storage temperatures

It is noteworthy that the solid-state cells exhibited better calendar aging properties at low or room temperatures; however, they are significantly vulnerable to the storage at a slightly higher temperature. In order to understand the noticeable degradation of the solid-state cell at high temperature, we closely examined the change in the redox activity of NCM811 cathode after the storage. Figure 3-6a–d presents differential capacity curves (vs voltage, dQ/dV) for solid-state cells at different conditions. It is well known that NCM811 electrode undergoes three phase transitions in the voltage window of 3.0–4.3 V (vs Li/Li^{+}); (i) layered hexagonal (H1) to monoclinic phase (M), (ii) monoclinic (M) to second hexagonal phase (H2), and (iii) second hexagonal (H2) to third hexagonal phase (H3),[38,39] as denoted with open circles, open triangles, and open diamonds, respectively, for the pristine cell in Figure 3-6a. Figure 3-6b and Figure 3-6c show that the solid-state cells that have been stored at 20 and 20 °C for six days still exhibit these characteristic redox peaks of NCM811, in consistent with the results of the galvanostatic cycle in Figure 3-5a and Figure 3-5c. On the contrary, the cell exposed to 70 °C [Figure 3-6d] displays a large polarization for each phase transition; that is, that of M↔H2 is markedly greater than those of other cells, and the H2↔H3 phase transition even disappears probably due to the excessively large polarization that caused the voltage cutoff in the cycle. Such large polarization is attributed to the detrimental porous cathode interface accompanied by the decomposition reaction, involving SO_x gas generation. We will discuss in detail later about the decomposition reaction through the characterization tools. The large polarization result of 70 °C solid-state cell also contrasts to the results of similar analysis on the cells employing liquid electrolyte in Figure 3-7a–d, which verified that, regardless of the storage conditions, typical three redox activities (H1↔M, M↔H2, and H2↔H3) were detected for all the cells with comparable polarization levels. The absence of H2↔H3 phase transition and the substantial voltage polarization for phase transitions particularly for the solid-state cell after 70 °C storage agrees with the significant reduction in the discharge capacity delivered in Figure 3-5a and implies that the loss of the capacity is likely due to the increase in the cell impedance occurring during the storage at 70 °C.

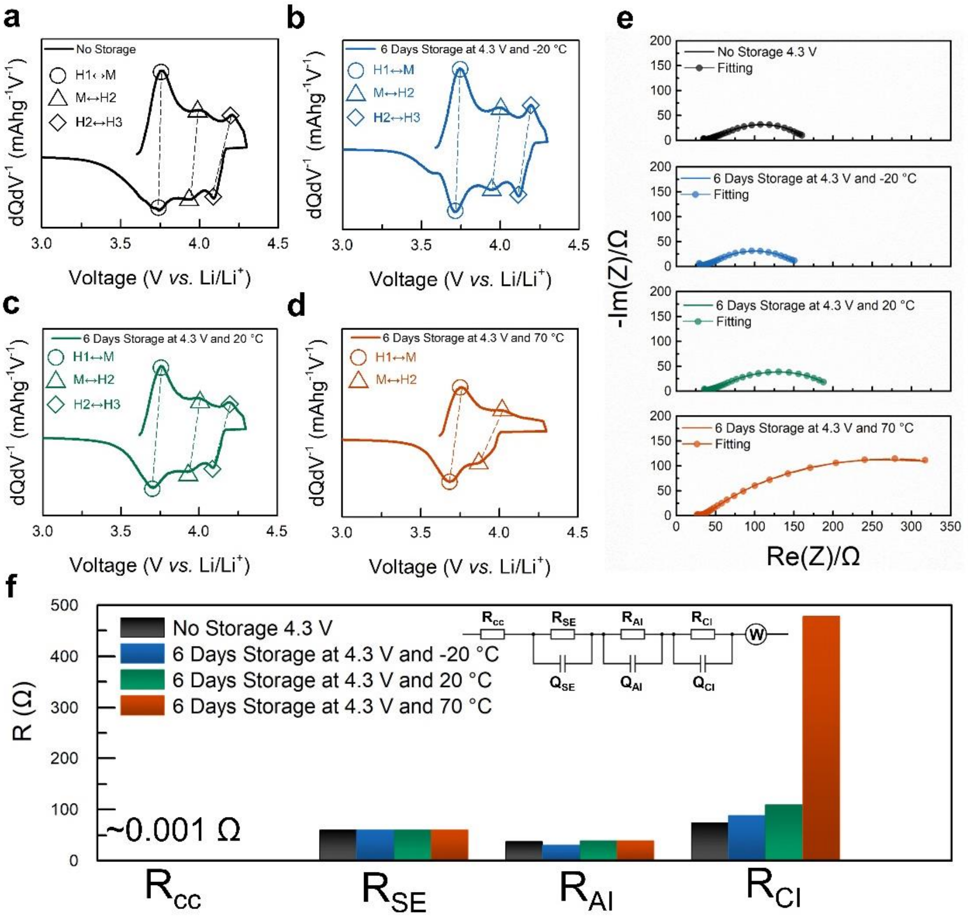

Figure 3-6. Differential capacity curves and electrochemical impedance spectra of 4.3 V charged solid-state cells in various storage temperatures. (a) dQ/dV graph of a solid-state cells at third cycle without storage. (b) dQ/dV graph of a solid-state cells at third cycle stored in −20 °C. (c) dQ/dV graph of a solid-state cell at third cycle stored in 20 °C. (d) dQ/dV graph of a solid-state cell at third cycle stored in 70 °C. (e) Electrochemical impedance spectra of −20, 20, and 70 °C stored solid-state cells. (f) Designated resistance values based on equivalent circuit of solid-state

cells. R_{CC}, R_{SE}, R_{AI}, and R_{CI} refer to resistance of current collector, solid electrolyte, anode interface, and cathode interface, respectively.

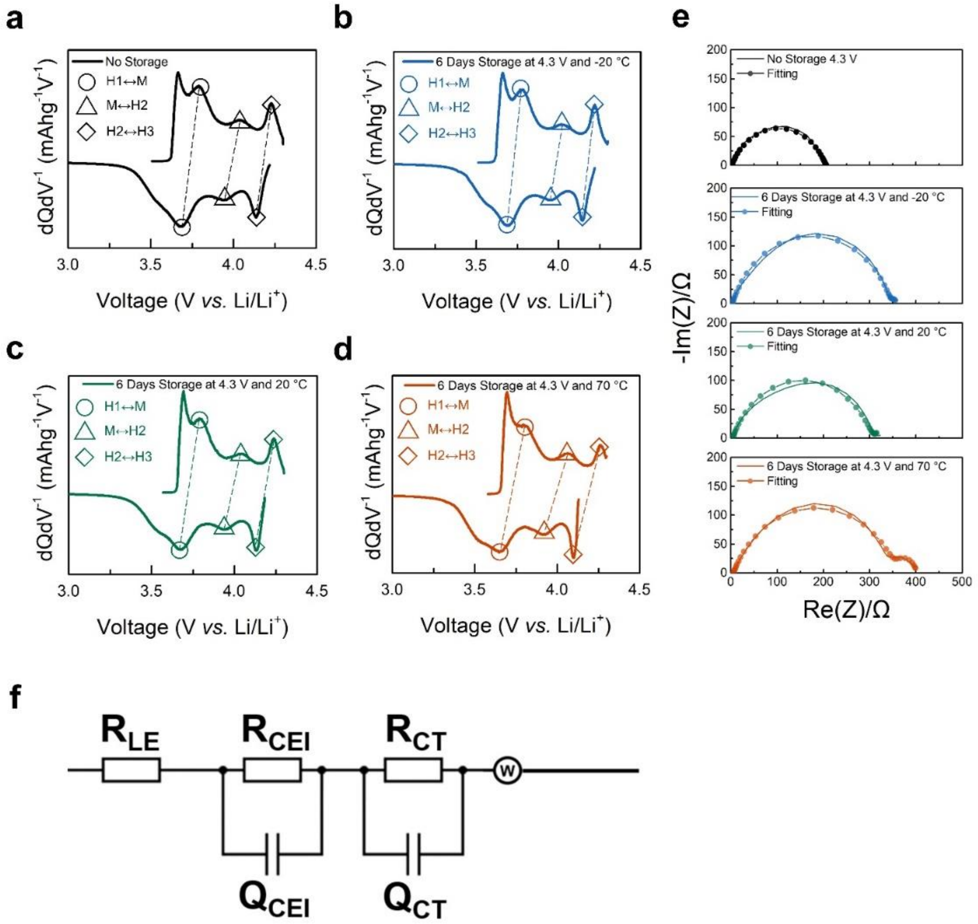

Figure 3-7. Differential capacity curves and electrochemical impedance spectra of 4.3 V charged liquid electrolyte batteries in various storage temperatures. a) dQ/dV graph of a liquid electrolyte cell at third cycle without storage. b) dQ/dV graph of a liquid electrolyte cell at third cycle stored in −20 °C. c) dQ/dV graph of a

liquid electrolyte cell at third cycle stored in 20 °C. d) dQ/dV graph of a liquid electrolyte cell at third cycle stored in 70 °C. e) Electrochemical impedance spectra of liquid electrolyte cells stored at −20, 20 and 70 °C for six days. f) Equivalent circuit of liquid electrolyte cells. R_{LE}, R_{CEI} and R_{CT} refer to resistance of liquid electrolyte, solid electrolyte, cathode electrolyte interface and charge transfer, respectively.

3.3.3 Electrochemical impedance spectroscopy analysis of solid-state and liquid electrolyte cells after various storage temperatures

In this respect, we carried out separate electrochemical impedance spectroscopy (EIS) analysis on the series of solid-state lithium cells, as presented in Figure 3-6e. It reveals that the overall impedance is maintained for the storage period as long as they are kept below room temperature (< 20 °C), whereas the solid-state cell stored at 70 °C shows significantly increased impedance. Such marked impedance increase was not observable for the cell employing the liquid electrolyte after the storage at 70 °C [Figure 3-7e], suggesting that the degradation with unexpectedly high impedance is unique to the solid-state cell. We found that the increased impedance of the solid-state cell is primarily attributable to the change in the cathode/electrolyte interface resistance according to the EIS data fitting with equivalent circuit employing four common resistance components (i.e., R_{cc}, R_{SE}, R_{AI}, and R_{CI}, representing the current collector resistance, bulk solid electrolyte resistance, anode, and cathode interfacial resistances, respectively), as presented in Figure 3-4f.[40] It unveils that the storage at 70 °C drastically increases the resistance particularly regarding the R_{CI}, compared with other resistance components. The cathode interface resistance increases by a factor of 6 from 74 Ω to about 470 Ω when stored at 70 °C for six days, while those of cells stored at –20 and 20 °C for the same period of the time maintained a similar level of R_{CI} at approximately 90 Ω. Detailed resistance values for decoupled circuit components are presented in Table 3-1, Figure 3-3, and 3.2.10 Detailed explanation on change in Li diffusion coefficients after the different storage conditions.

	4.3 V Fresh	**-20 °C 4.3 V Rest 6 Days**	**20 °C 4.3 V Rest 6 Days**	**70 °C 4.3 V Rest 6 Days**
R_{CC}	0.001 Ω	0.001 Ω	0.001 Ω	0.001 Ω
Q_{SE}	1.44×10^{-3} Fs	1.385×10^{-3} Fs	4.455×10^{-3} Fs	3.917×10^{-3} Fs
R_{SE}	60 Ω	60 Ω	60 Ω	60 Ω
Q_{AI}	0.271×10^{-6} Fs	0.37×10^{-9} Fs	0.254×10^{-6} Fs	0.833×10^{-3} Fs
R_{AI}	37.12 Ω	29.44 Ω	38.17 Ω	38.00 Ω
Q_{CI}	3.278×10^{-3} Fs	5.515×10^{-3} Fs	1.985×10^{-3} Fs	2.043×10^{-3} Fs
R_{CI}	74.01 Ω	87.57 Ω	108.9 Ω	476.8 Ω

Table 3-1. Detailed values of designated resistance and capacitances based on equivalent circuit of all-solid-state batteries.

3.3.4 X-ray diffraction analysis of solid-state cells after various storage temperatures

In order to elucidate the origin of the abnormal growth of the cathode interface impedance, XRD analysis was comparatively carried out for composite cathodes stored at different temperatures, during the period of storage at every three days. The series of XRD patterns collected during the storage are presented for the composite cathodes (charged at 4.3 V) stored at 20, 70, and –20 °C in Figure 3-8a, Figure 3-8b, and Figure 3-9, respectively. All the pristine composite cathodes exhibit typical features of NCM811 such as (003), (101) and (104) peaks, while main XRD peaks of Li_6PS_5Cl are clearly observable 2θ = 24–36° as indicated with filled downward triangle symbol.[3,41,42] Upon charging to 4.3 V, the (003) peak of NCM811 shifts to a higher 2θ angle, indicating the delithiation of NCM811 cathode and the formation of H3 phase, which is consistently detected for all the composite cathodes [Figure 3-8c, Figure 3-8e, and Figure 3-10].[43,44] Interestingly, we found that the NCM811 cathode undergoes minor self-discharge reaction during the storage period, as evidenced by the gradual shift of (003) peak to a smaller 2θ angle in Figure 3-8c and Figure 3-8e. The degree of the self-discharge slightly increased with the temperature of the storage, which agrees with the observed tendency of the coulombic efficiencies during the initial cycle right after the storage in Figure 3-1. Nevertheless, it should be noted that the capacity loss from the self-discharge could be recovered after the initial cycle for all the samples, and does not explain the continued difference of capacities in the subsequent cycles in Figure 3-5c. More importantly, it was found that the main peaks of Li_6PS_5Cl notably shifted to larger 2θ angles after the 4.3 V charging of the composite cathodes, indicating the electrochemical activity of the electrolyte to some extent. In order to confirm this, *ex situ* XRD analysis was carried out in our separate experiment, as presented in Figure 3-10c, and it verified that the Li_6PS_5Cl peaks gradually shift with the charging of the composite cathode up to 4.3 V. It is indicative of the delithiation of Li_6PS_5Cl phase involving the change in the average lattice parameters, which has been recently observed experimentally and theoretically by Schwietert *et al.*, and was pointed as enabling the stable solid-state cell operations without electrolyte degradation.[3,42,45,46] It is also consistent with our observations that the metastable delithiated argyrodite ($Li_{6-x}PS_5Cl$) phase could be well maintained even after the six-day storage at 20 and –20 °C [Figure 3-8d and Figure 3-9c]. Nonetheless, our findings here indicate that the stability of the delithiated argyrodite phase can be remarkably different depending on the storage temperature that it was exposed to. Unlike the cases of aging at 20 and –20 °C, the delithiated argyrodite phase in the 70 °C stored composite cathode was witnessed to undergo a significant phase evolution over time. The XRD spectra in Figure 3-8f illustrate that the characteristic peaks of the argyrodite phase disappear after three days, and new sets of peaks begin to emerge, which are consistently observed after six days. The new peaks were identified to be corresponding to LiCl, S, and Li_3PS_4, indicating that the phase transition is likely to be irreversible [Figure 3-8f].[3,45,46] In addition, after six days, the peaks corresponding to sulfur-containing by-products (S and Li_3PS_4) become significantly weakened, implying that these decomposition products tend to partially amorphize during the extended high-temperature storage.

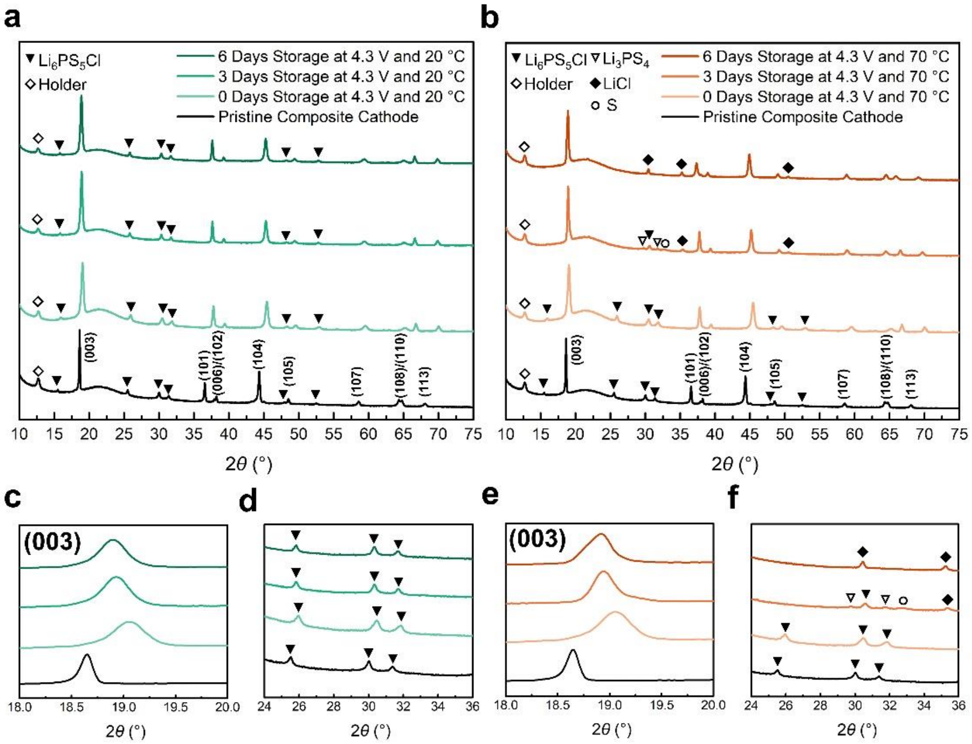

Figure 3-8. X-ray diffraction analysis of 4.3 V charged all-solid-state battery stored under 20 and 70 °C. (a) XRD analysis of 4.3 V charged solid-state cells from zero to six days storage under 20 °C. Filled downward triangle and open diamond symbols refer to Li_6PS_5Cl and holder, respectively. (b) XRD analysis of 4.3 V charged solid-state cells from zero to six days of storage under 70 °C. Filled downward triangles, open downward triangles, open diamonds, filled diamonds, and open circle symbols refer to Li_6PS_5Cl, Li_3PS_4, holder, LiCl, and S, respectively. (c) (003) peak shift of 4.3 V charged NCM811 from zero to six days of storage under

20 °C (2θ = 18–20). (d) Main peak shift of Li_6PS_5Cl from zero to six days of storage under 20 °C (2θ = 24–36). (e) 003 peak shift of 4.3 V charged NCM811 from zero to six days of storage under 70 °C (2θ = 18–20). (f) Main peak decomposition of Li_6PS_5Cl from zero to six days of storage under 70 °C (2θ = 24–36).

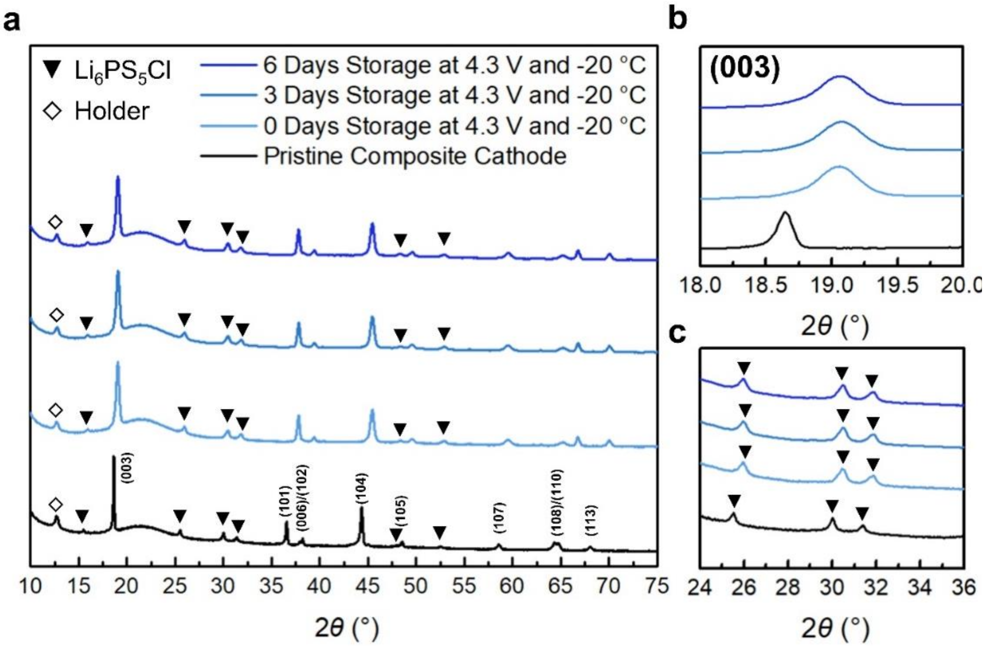

Figure 3-9. X-ray Diffraction analysis of 4.3 V charged all-solid-state battery stored under –20 °C. a) XRD analysis of 4.3 V charged solid-state cells from 0 to 6 days storage under –20 °C. b) (003) peak shift of 4.3V charged NCM811 from 0 to 6 days storage under –20 °C (2θ = 18 – 20). c) Main peak shift of Li_6PS_5Cl from 0 to 6 days storage under –20 °C (2θ = 24 – 36).

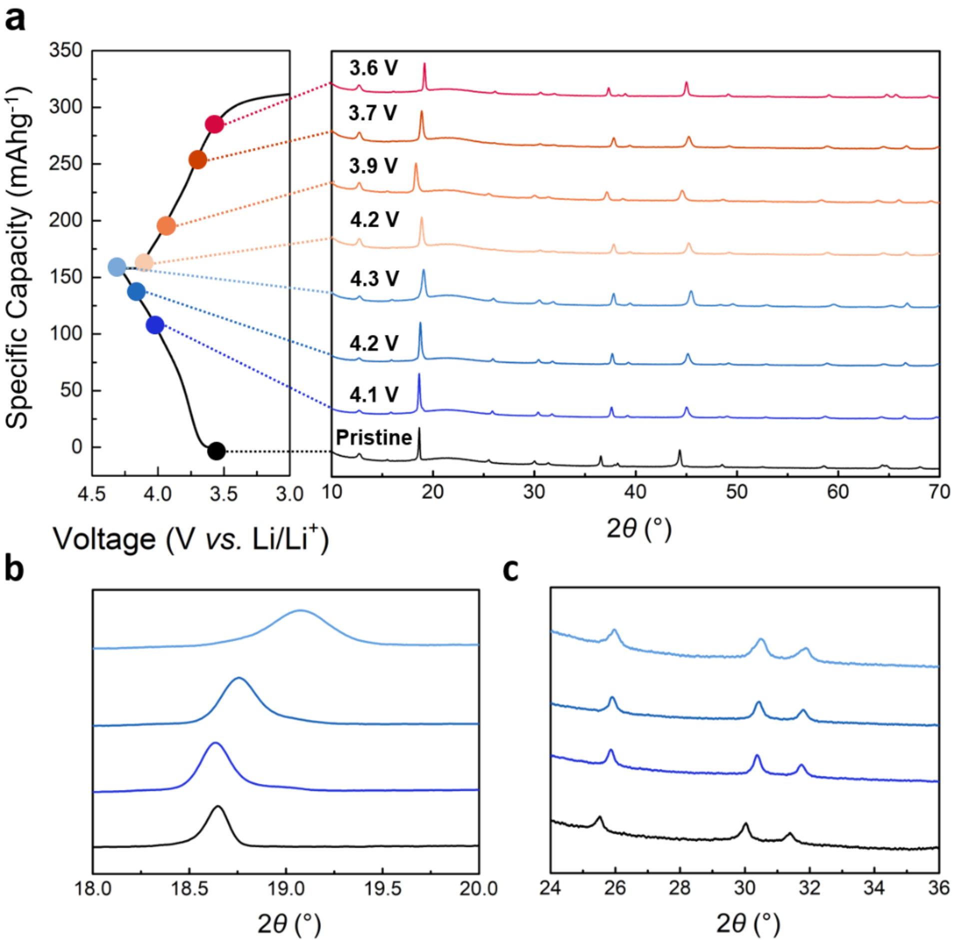

Figure 3-10. *Ex-situ* XRD of NCM811 solid-state cells in operation voltage window of 3.0 – 4.3 V. (a) *ex-situ* XRD analysis of NCM811 solid-state cells at 0.1 C rate. b) (003) peak shift of NCM811 solid-state cells from pristine to 4.3 V (2θ = 18 – 20). c) Main peak shift of Li_6PS_5Cl from pristine to 4.3 V (2θ = 24 – 36).

3.3.5 Li_6PS_5Cl–C electrode solid-state cell storage and reassembly of NCM811 solid-state cell for exclusion of NCM811 influence in the storage effect

In order to more clearly confirm the decomposition of the Li_6PS_5Cl and demonstrate its effect, we prepared the electrode solely composed of Li_6PS_5Cl and carbon (10:1 in weight ratio) and charged it in a half-cell to 4.3 V, as schematically shown in Figure 3-11a. Subsequently, the 4.3 V charged Li_6PS_5Cl–C electrodes were stored at 20 and 70 °C, respectively, for six days. In accordance with the results in Figure 3-8 and the previous literature,[3] the Li_6PS_5Cl electrode exhibited the electrochemical activity, delivering non-negligible amount of capacity through the delithiation process. Figure 3-11b displays how the delithiated argyrodite phase evolves upon six-day storage at different temperatures. It evidently confirms that the argyrodite phase undergoes a noticeable decomposition selectively with the high temperature exposure. The XRD patterns depict that the aging at 70 °C results in the partial decomposition of the delithiated argyrodite phase, yielding LiCl, S, and Li_3PS_4 by-products, whereas it remains relatively stable when aged in 20 °C. It strongly suggests the vulnerability of the delithiated argyrodite electrolyte in the composite cathode to the high-temperature storage. Regarding the partial decomposition in this experiment, we suppose that only a fraction of Li_6PS_5Cl could be delithiated with the aid of the carbon additives in the composite electrode due to the low electronic conductivity of the Li_6PS_5Cl, thereby leaving some unreacted Li_6PS_5Cl phase in the sample.

Using these two Li_6PS_5Cl–C electrode samples after aging, we further investigated how the degraded Li_6PS_5Cl electrolyte would have an influence on the electrochemical performance of the NCM811 cathode by reassembling the solid-state cells. First, we reground the Li_6PS_5Cl–C composite electrodes that underwent the aging experiments, mixed it with fresh NCM811 powder to prepare NCM811 composite cathode again, keeping the overall carbon contents of the electrode the same as the original case, and reassembled solid-state cells for electrochemical tests. As shown in Figure 3-11c, to our surprise, the reassembled solid-state cells operated at room temperature displayed the similar trend of the cell-storage effect, which has been observed during aging of the entire solid-state cells at different temperatures. The cell reassembled with the 70 °C stored Li_6PS_5Cl exhibited a large voltage hysteresis with the substantially reduced capacity, while that with the 20 °C stored Li_6PS_5Cl showed a similar level of capacity/polarization with the reference solid-state cell, which is analogous to the findings in Figure 3-5a. This clearly demonstrates the loss of the deliverable capacity along with the buildup of the polarization observed for the aged solid-state cell is primarily attributable to the degradation of the Li_6PS_5Cl, which undergoes irreversible decomposition into LiCl, S, and Li_3PS_4 upon the high-temperature storage at the delithiated state, thereby failing to serve as a proper lithium-ion conductor for solid-state cell operation.

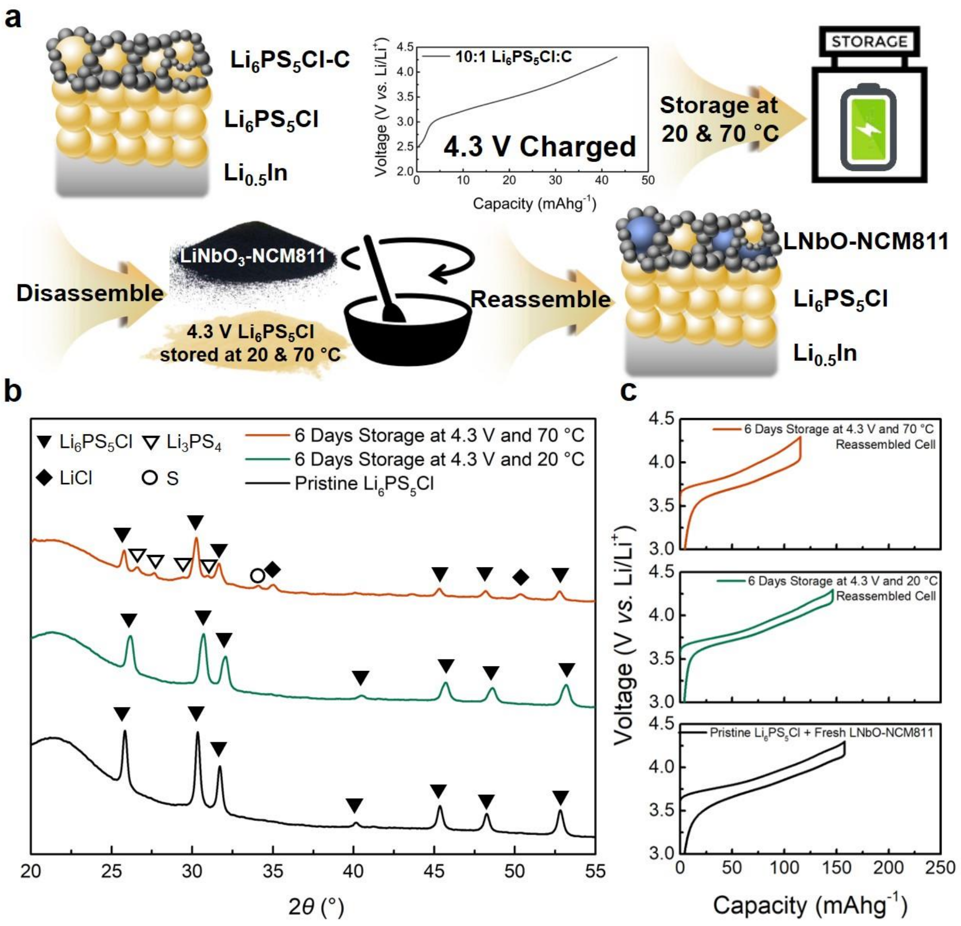

Figure 3-11. X-ray diffraction analysis and polarization examination of 4.3 V charged Li_6PS_5Cl stored under 20 and 70 °C. (a) Schematics of experiments related to 4.3 V charged Li_6PS_5Cl. (b) XRD analysis of 4.3 V charged Li_6PS_5Cl stored under 20 and 70 °C for six days. (c) Second charge/discharge profiles of reference cell, 4.3 V charged Li_6PS_5Cl stored under 20 and 70 °C reassembled cells.

3.3.6 X-ray absorption near edge spectroscopy analysis for oxidations states of S^{2-}, P^{5+} and Cl^{-} in Li_6PS_5Cl

We decided to further probe the changes in the Li_6PS_5Cl structure and the nature of the decomposition products, employing X-ray absorption near edge spectroscopy (XANES) analysis. Figure 3-12a–c display the XANES spectra at sulfur K-edge, phosphorus Kedge, and chlorine K-edge, respectively, for the 4.3 V charged NCM811 composite cathodes after the storage at different temperatures. It shows that appreciable oxidations of both sulfur and phosphorous have taken place, whereas the oxidation state of chlorine remains unchanged. Considering that the delithiated Li_6PS_5Cl was partly responsible for the de-lithiation of the composite cathode and was relatively stable in –20 and 20 °C storage cases, it indicates that the redox activity of Li_6PS_5Cl originates from the partial oxidation of both sulfur and phosphorous. Compared with pristine Li_6PS_5Cl, XANES spectra at sulfur and phosphorus K-edges of –20 and 20 °C stored cathodes shift to higher energies, indicating S^{2-} and P^{5+} to higher oxidation states. The slight oxidation of sulfur at K-edge of 20 and 20 °C stored cases is in agreement with the previously reported works on the delithiated argyrodite.[47] On the other hand, XANES spectra of the 70 °C stored case suggest that both the sulfur and phosphorous are back in reduced states. The sulfur K-edges recover the original position of the Li_6PS_5Cl, inferring that the delithiated argyrodite, harboring oxidized S^{2-} through charging process, has been reduced after the 70 °C storage. In the case of the phosphorous, the shift of K-edges indicates that the reduction has similarly occurred; however, its edge energy is slightly deviated from the original position. While the origin of this shift is not clear, it strongly suggests that the reduction of phosphorous yields a P^{4+}-containing by-product that significantly differs from the original Li_6PS_5Cl phase. These findings indicate that oxidation/reduction of sulfur and phosphorus is responsible for the formation of metastable delithiated argyrodite, and its decomposition at the 70 °C storage involves significant valence changes.

3.3.7 Thermogravimetric with mass spectrometer analysis for gas evolution during the storage at elevated temperature

During the course of investigating the decomposition route of the $Li_{6-x}PS_5Cl$, we unexpectedly found that it also involves the gas evolution, which could not be detected either in XRD and XANES characterization, from the thermogravimetric analysis with mass spectrometer (TGA-MS). In this analysis, the decomposition reaction of the $Li_{6-x}PS_5Cl$ was monitored by systematically increasing the temperature to 90 °C with Ar flow, measuring the mass change, heat flow and gas generation, as displayed in Figure 3-12d. According to derivative thermogravimetry (DTG) curve in the figure, the major change in mass is observed at around 63 °C, indicating the phase transition involving gas generation at the temperature. It is consistent with the differential scanning calorimetry (DSC), which detects a major heat flow at around 63 °C. More importantly, we could directly probe the evolution of the gas species with specific mass-to-charge ratios (*m/z*), maximizing at around 63 °C. The observed *m/z* values of 48 and 64 correspond to SO and SO_2, respectively, demonstrating the general SO_x gas evolution at this temperature. These TGA-MS results unequivocally elucidate why the 70 °C storage was critical to the charged solid-state cell containing the delithiated $Li_{6-x}PS_5Cl$ argyrodite phase. When the composite cathode is charged in the solid-state cell, the Li_6PS_5Cl argyrodite phase is also accordingly delithiated, forming the metastable $Li_{6-x}PS_5Cl$ argyrodite phase, which, upon exposure to higher temperature than ~ 63 °C, decomposes involving the gas generation of SO_x along with the formation other byproducts such as LiCl, S and Li_3PS_4.

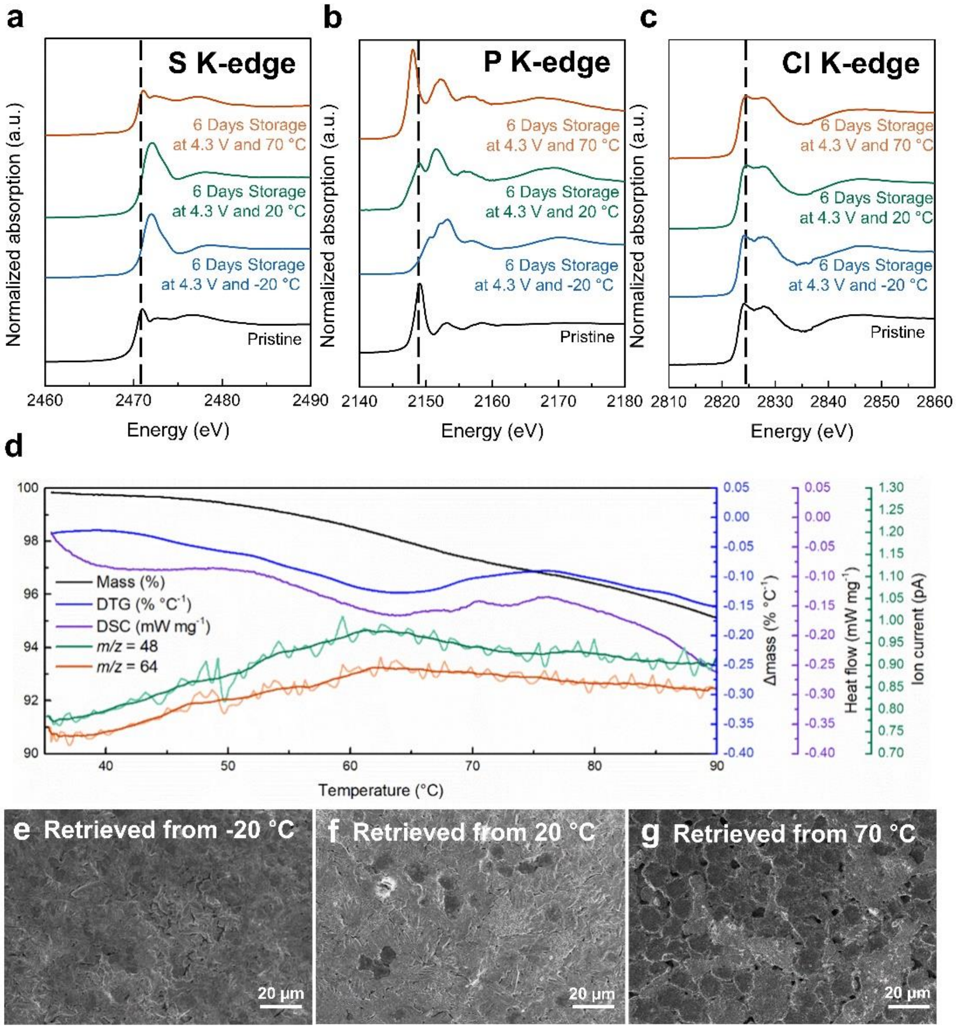

Figure 3-12. XANES spectra and morphology change followed by gas evolution of 4.3 V charged all-solid-state batteries stored under various temperatures. (a) XANES at sulfur Kedge spectra of 4.3 V charged solid-state cells stored under –20, 20, and 70 °C. (b) XANES spectra at phosphorus K-edge of 4.3 V charged solid-state cells stored under –20, 20, and 70 °C. (c) XANES spectra at chlorine K-edge of 4.3 V charged solid-state cells stored under – 20, 20, and 70 °C. (d) TGA-MS

graph for 4.3 V charged NCM811 composite cathode showing relative sample mass loss, mass loss rate, heat flow, and ion current on m/z = 48 and m/z = 64. (e) SEM image of 4.3 V charged NCM811 composite cathode stored at –20 °C for six days. (f) SEM image of 4.3 V charged NCM811 composite cathode stored at 20 °C for six days. (g) SEM image of 4.3 V charged NCM811 composite cathode stored at 70 °C for six days

3.3.8 Observation of morphological change of NCM811 solid-state cells after the various storage temperatures

Then, the remaining questions are: (i) what are the source of oxygen in the formation of SO_x and (ii) why a small amount of the gas evolution can possibly lead to a drastic increase in the cathode/electrolyte interface impedance, thereby leading to the significant capacity reduction. We suppose that the oxygen is taken from the delithiated NCM811 surface, considering there is no other oxygen source present in the composite cathodes. It is well-known that the oxide cathodes with high nickel contents tend to liberate the lattice oxygen when highly charged[48–51], and it is supposed that it reacted with the delithiated argyrodite phase, forming SO_x during the extended elevated-temperature storage.

In order to confirm the suggested degradation mechanism above, two additional experiments were carried out. First, the electrochemical performances of NCM811 ASSB operated under 20 and 70 °C are also compared. Figure 3-13 illustrates that the solid-state cell at 70 °C shows a significantly high irreversible capacity of ~150 $mAhg^{-1}$, which contrasts to the case of 20 °C operations. It is consistent with our findings on the electrochemical instability of Li_6PS_5Cl at delithiated state upon the temperature elevation. Indeed, we could indirectly verify the gas evolution from the decomposition of delithiated Li_6PS_5Cl during cycles, by probing the pressure gauge as shown in Figure R2b. The solid-state cells were packaged in air-tight container with Ar atmosphere and partially vacuumed (~ –0.06 MPa), and the change in the pressure was monitored during the cycling of the cells. It presents that the pressure of solid-state cell gradually increases from –0.06 MPa to ~ –0.02 MPa after 20 cycles at 70 °C, implying that SO_x gas has been generated during charging/discharging at 70 °C. In Figure R2d, we also compared the cycle life of solid-state cells operated at 0.1 C under 20 and 70 °C, respectively. It presents that the NCM-sulfide solid-state cell is stably operated at 20 °C, delivering approximately ~140 $mAhg^{-1}$ discharge capacity after 20 cycles. On the other hand, 70 °C-operated ASSB exhibits faster degradation of the capacity, retaining only ~80 $mAhg^{-1}$ of capacity after 20 cycles. This is consistent with the results of our storage-experiment at different temperature, showing the vulnerability of the delithiated Li_6PS_5Cl at high temperature.

Second, we have examined electrochemical performance of solid-state cells employing $LiCoO_2$ cathode after six days of 20 and 70 °C storages. The upper cutoff operation voltage for $LiCoO_2$ was limited to 4.2 V, because extracting/inserting more than 0.5 Li^+ per $LiCoO_2$ often leads to a rapid capacity fade. Other conditions of the storage or details of cell manufacture were kept identical to the original experiment as stated in experimental section. In order to monitor the gas generation during the storage, a pressure gauge was mounted to solid-state cells as illustrated in Figure 3-14. The solid-state cell was packaged in air-tight container with Ar atmosphere and partially vacuumed (~ –0.07 MPa) as shown in the figure. Subsequently, the partially vacuumed package was stored in a 70 °C-chamber for six days. After six days of storage under 70 °C, we found that the pressure increased to ~ –0.055 MPa, implying the gas evolution during the 70 °C (Figure R6b). Moreover, the electrochemical performances were compared after the six days of 20 and 70 °C-storage. Figure 3-14c comparatively presents the electrochemical profiles of the two samples. It shows that the voltage hysteresis has notably increased with the case of the 70°C storage. The discharge capacity also substantially decreased from ~110 mAhg^{-1} to ~80 mAhg^{-1}, referring that the delithiated Li_6PS_5Cl still undergoes the decomposition with SO_x gas generation. Moreover, the compromised discharge capacity was prolonged throughout the cycle life, which is the similar trend as shown in Figure 1c. It clearly indicates that the instability issue of the delithiated Li_6PS_5Cl is persistent and would arise regardless of the type of oxide cathode materials.

Considering that the gas evolution should start from the interface from the NCM811 surface and the argyrodite phase, we reasoned that it can cause physical disconnection between the two, leading to the increase in the interfacial resistance during the electrochemical reaction. Accordingly, we carefully examined the morphological change in the NCM811/electrolyte interface in the composite cathode after the storage experiments. Figure 3-12e–g are SEM images of NCM811 composite cathodes (charged at 4.3V) retrieved from the six-day storage at –20 °C, 20 °C and 70 °C. The –20 °C and 20 °C stored composite cathodes exhibit compact interface, offering intimate contact between NCM811 and Li_6PS_5Cl. However, it was notably found that 70 °C stored composite cathode displays extensively porous interface between NCM811 and Li_6PS_5Cl, losing the physical connectivity in the composite cathode. This appreciable morphological interface degradation is highly likely to lead to the abnormal growth in the interfacial resistance. Additionally, we found that this detrimental porous cathode interface is consistently observed in the composite cathodes even after 10 cycles (Figure 3-15 and Figure 3-16), which would continue to contribute to the high impedance and the low capacity throughout the cycle

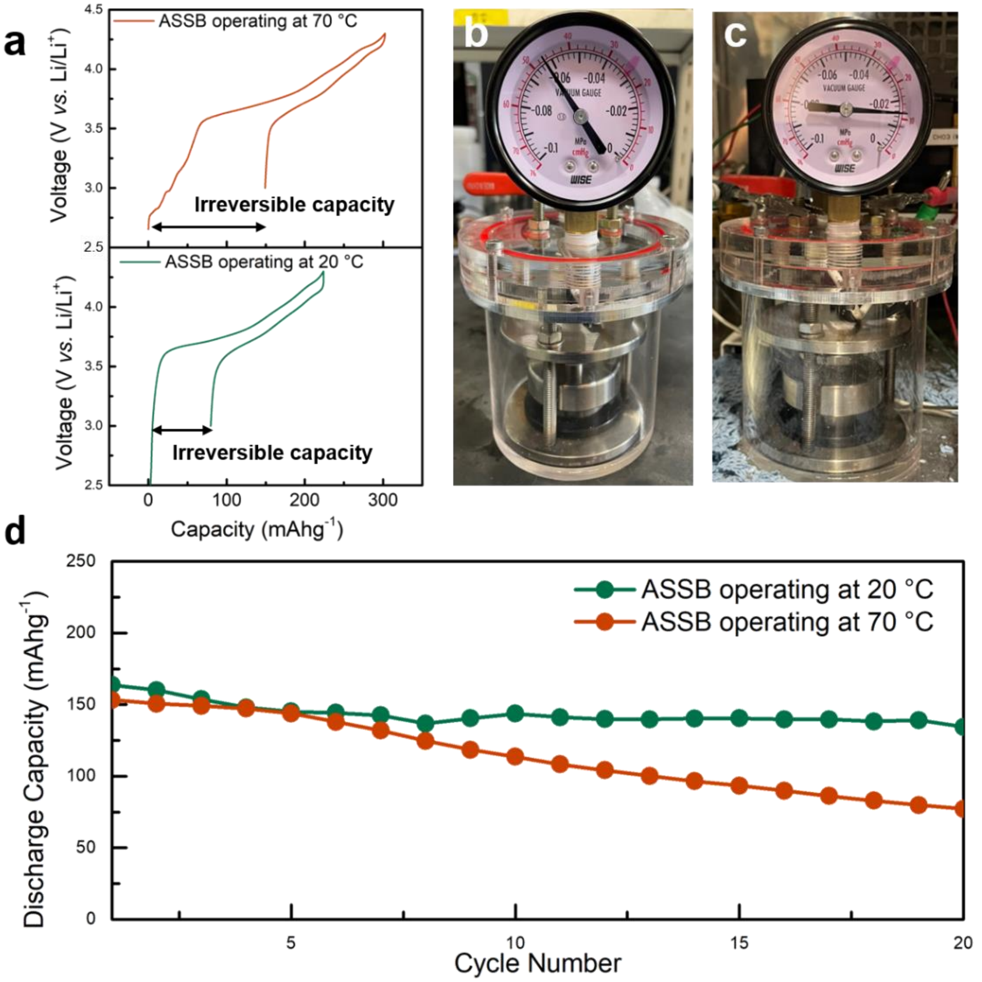

Figure 3-13. Electrochemical performance of ASSBs operating at 20 and 70 °C. a) First cycle profile of ASSBs operating at 0.1 C under 20 and 70 °C. b) Partially vacuumed ASSB package at pristine state. c) Dropped vacuum level of ASSB package after 20 cycles under 70 °C operating temperature. d) Cycle life of ASSBs at 0.1 C under 20 and 70 °C operating temperatures.

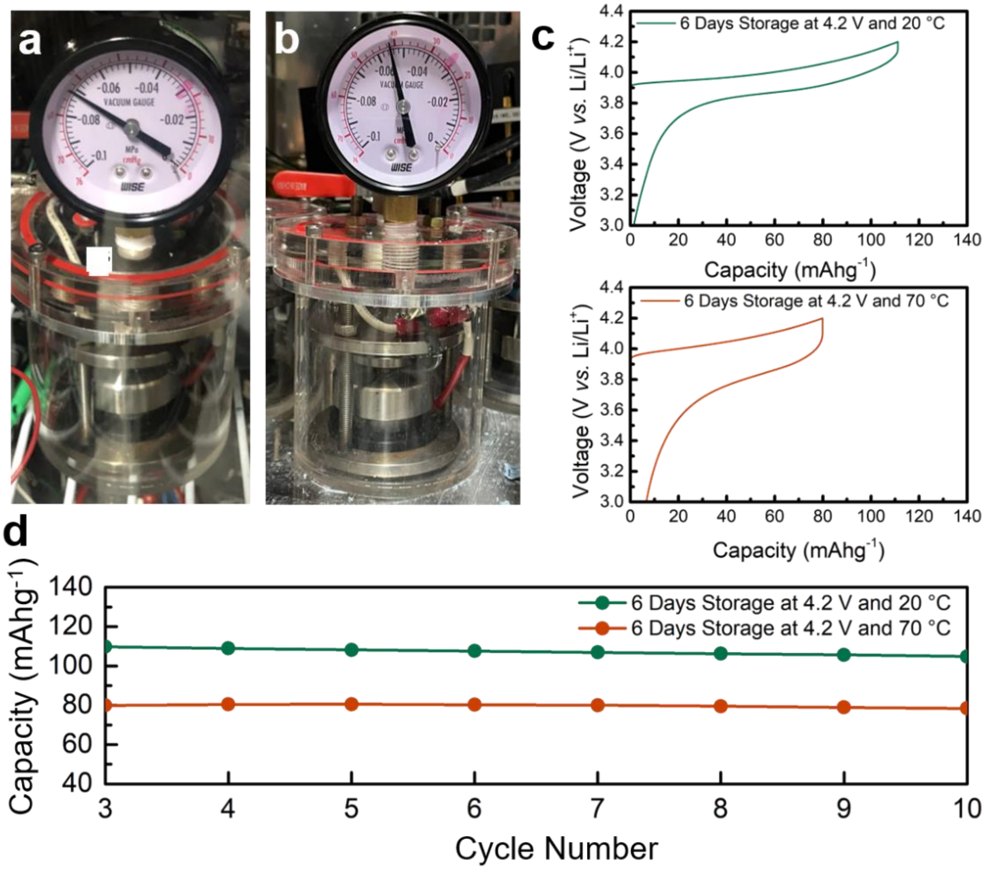

Figure 3-14. Electrochemical performance of ASSBs operating at 20 and 70 °C. a) Partially vacuumed 4.2 V charged ASSB package before 70 °C-storage. b) Dropped vacuum level of 4.2 V charged ASSB package after 6 days of 70 °C-storage c) Third cycle charge/discharge profile of 4.3 V charged ASSBs after 20 and 70 °C-storage for six days. d) Cycle life of ASSBs at 0.1 C under 20 and 70 °C.

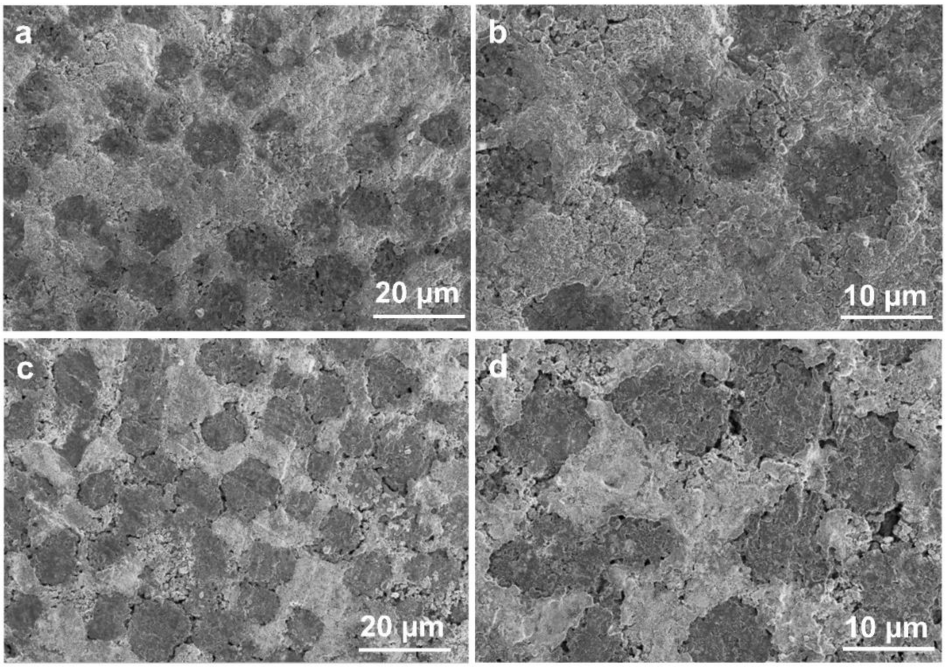

Figure 3-15. SEM images of composite cathode in solid-state cells stored at –20 °C and 70 °C after 10 cycles. a–b) 4.3V charged NCM811 composite cathode stored at –20 °C for six days after 10 cycles. c–d) 4.3V charged NCM811 composite cathode stored at 70 °C for six days after 10 cycles. All samples are stored under vacuum/Ar atmosphere

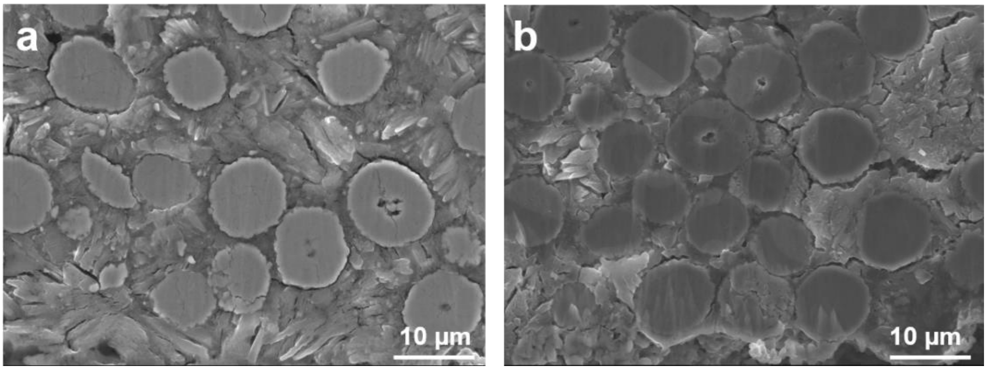

Figure 3-16. **Cross-section SEM images of 4.3 V charged NCM811 composite cathode stored at a) -20 and b) 70 °C.**

3.4 Concluding remarks

We investigated the reliability of Li_6PS_5Cl-based ASSB system in practically harsh but plausible storage conditions, and report, for the first time, that a substantial deterioration of ASSB can occur after the high-temperature storage as low as 70 °C. From the extensive characterizations, we brought to light that this degradation is correlated with the corrosion of the cathode/Li_6PS_5Cl interface, which arises due to the thermal instability of the delithiated argyrodite phase, developing a detrimental porous interface structure that results in the physical particle-to-particle disconnect in the composite cathode. It indicates that the stability of the solid electrolyte, which has been believed to be failsafe, needs to be carefully revisited at various practical operational conditions for actual applications in ASSBs. Moreover, our work suggests that future research efforts should be placed in developing effective strategies to overcome various issues with the storage of ASSBs in real-world environments concerning not only the temperatures, SOCs and/or C-rate but also various operating patterns.

3.5 References

1. Zhu, F. *et al.* Single-atom-layer traps in a solid electrolyte for lithium batteries. *Nat. Commun.* **11**, 1828 (2020).
2. Wang, M. J. *et al.* Enabling "lithium-free" manufacturing of pure lithium metal solid-state batteries through in situ plating. *Nat. Commun.* **11**, 5201 (2020).
3. Schwietert, T. K. *et al.* Clarifying the relationship between redox activity and electrochemical stability in solid electrolytes. *Nat. Mater.* **19**, 428 (2020).
4. Kim, S. *et al.* The Role of Interlayer Chemistry in Li-Metal Growth through a Garnet-Type Solid Electrolyte. *Adv. Energy Mater.* **10**, 1903993 (2020).
5. Hayashi, A. *et al.* A sodium-ion sulfide solid electrolyte with unprecedented conductivity at room temperature. *Nat. Commun.* **10**, 5266 (2019).
6. Tarascon, J. M. & Armand, M. Issues and challenges facing rechargeable lithium batteries. *Nature* **414**, 359 (2001).
7. Pfenninger, R. *et al.* A low ride on processing temperature for fast lithium conduction in garnet solid-state battery films. *Nat. Energy* **4**, 475 (2019).
8. Baird, A. R. *et al.* Explosion hazards from lithium-ion battery vent gas. *J. Power Sources* **446**, 227257 (2020).
9. Wang, Q. *et al.* Thermal runaway caused fire and explosion of lithium ion battery. *J. Power Sources* **208**, 210 (2012).

10. Feng, X. *et al.* Thermal runaway mechanism of lithium ion battery for electric vehicles: A review. *Energy Storage Mater.* **10**, 246 (2018).

11. Guirong, Z. & Henghai, Z. Research of the electric vehicle safety. *World Autom. Congr.* 1 (2012).

12. Shin, D. O. *et al.* Synergistic multi-doping effects on the $Li_7La_3Zr_2O_{12}$ solid electrolyte for fast lithium ion conduction. *Sci. Rep.* **5** (1), 1 (2015).

13. Kim, J.-J., Yoon, K., Park, I. & Kang, K. Progress in the Development of Sodium-Ion Solid Electrolytes. *Small Methods* **1**, 1700219 (2017).

14. Chang, D., Oh, K., Kim, S. J. & Kang, K. Super-ionic conduction in solid-state $Li_7P_3S_{11}$-type sulfide electrolytes. *Chem. Mater.* **30**, 8764 (2018).

15. Xu, L. *et al.* Interfaces in solid-state lithium batteries. *Joule* **2**, 1991 (2018).

16. Yoon, K., Kim, J.-J., Seong, W. M., Lee, M. H. & Kang, K. Investigation on the interface between $Li_{10}GeP_2S_{12}$ electrolyte and carbon conductive agents in all-solid-state lithium battery *Sci. Rep.* **8**, 1 (2018).

17. Lee, Y.-G. *et al.* High-energy long-cycling all-solid-state lithium metal batteries enabled by silver–carbon composite anodes *Nat. Energy* **5**, 299 (2020).

18. Kato, Y. *et al.* High-power all-solid-state batteries using sulfide superionic conductors. *Nat. Energy* **1**, 16030 (2016).

19. Lee, K. *et al.* Multifunctional Interface for High-Rate and Long-Durable Garnet-Type Solid Electrolyte in Lithium Metal Batteries. *Energy Lett.* **7**, 381 (2022).

20. Yoon, K., Lee, S., Oh, K. & Kang, K. Challenges and Strategies towards Practically Feasible Solid-State Lithium Metal Batteries. *Adv. Mater.* **34**, 2104666 (2022).

21. Cao, D., Sun, X., Li, Q., Natan, A., Xiang, P., & Zhu, H. Lithium Dendrite in All-Solid-State Batteries: Growth Mechanisms, Suppression Strategies, and Characterizations. *Matter* **3**, 57 (2020).

22. Whiteley, J. M., Woo, J. H., Hu, E., Nam, K.-W. & Lee, S.-H. Empowering the lithium metal battery through a silicon-based superionic conductor. *J. Electrochem. Soc* **161** (12), A1812 (2014).

23. Liang, B. *et al.* Preparation and characterization of PEO-PMMA polymer composite electrolytes doped with nano-Al2O3. *Electrochim. Acta* **169**, 334 (2015).

24. Wenzel, S. *et al.* Interphase formation and degradation of charge transfer kinetics between a lithium metal anode and highly crystalline $Li_7P_3S_{11}$ solid electrolyte. *Solid State Ion.* **286**, 24 (2016).

25. Ma, J., Chen, B., Wang, L. & Cui, G. Progress and prospect on failure mechanisms of solid-state lithium batteries. *J. Power Sources* **392**, 94 (2018).

26. Grundstein, A., Meentemeyer, V. & Dowd, J. Maximum vehicle cabin temperatures under different meteorological conditions. *Int. J. Biometeorol.* **53**, 255 (2009).

27. Wu, Y. *et al.* Progress in thermal stability of all-solid-state-Li-ion-batteries. *InfoMat* **3**, 827 (2021).

28. Hu, G. *et al.* Enhanced Electrochemical Properties of $LiNi_{0.8}Co_{0.1}Mn_{0.1}O_2$ Cathode Materials Modified with Lithium-Ion Conductive Coating $LiNbO_3$. *ChemElectroChem* **6**, 4773 (2019).

29. Li, X. *et al.* $LiNbO_3$-coated $LiNi_{0.8}Co_{0.1}Mn_{0.1}O_2$ cathode with high discharge capacity and rate performance for all-solid-state lithium battery. *J. Energy Chem.* **40**, 39 (2020).

30. Hu, D. *et al.* High-Temperature Storage Deterioration Mechanism of Cylindrical 21700-Type Batteries Using Ni-Rich Cathodes under Different SOCs. *ACS Appl. Mater. Interfaces* **13**, 6286 (2021).

31. Schmitt, J. *et al.* Impedance change and capacity fade of lithium nickel manganese cobalt oxide-based batteries during calendar aging. *J. Power Sources* **353**, 183 (2017).

32. Liao, X. *et al.* Understanding self-discharge mechanism of layered nickel cobalt manganese oxide at high potential. *J. Power Sources* **286**, 551 (2015).

33. Keil, P. *et al.* Calendar aging of lithium-ion batteries. *J. Electrochem. Soc* **163** (9), A1872 (2016).

34. Ryu, H. H., Park, G. T. , Yoon, C. S. & Sun, Y. K. Microstructural Degradation of Ni-Rich Li[$Ni_xCo_yMn_{1-x-y}$]O_2 Cathodes During Accelerated Calendar Aging. *Small* **14**, 1803179 (2018).

35. Balagopal, B., Huang, C. S. & M. Chow, in *2018 IESES* (IEEE, 2018), p. 32.

36. Wood, S. M. *et al.* Predicting Calendar Aging in Lithium Metal Secondary Batteries: The Impacts of Solid Electrolyte Interphase Composition and Stability. *Adv. Energy Mater.* **8**, 1801427 (2018).

37. Seong, W. M. *et al.* Abnormal self-discharge in lithium-ion batteries. *Energy Environ. Sci.* **11**, 970 (2018).

38. Kim, J.-H. *et al.* A method of increasing the energy density of layered Ni-rich Li[$Ni_{1-2x}Co_xMn_x$]O_2 cathodes (x= 0.05, 0.1, 0.2). *J. Mater. Chem. A* **7**, 2694 (2019).

39. Zhang, S. S. Understanding of performance degradation of $LiNi_{0.80}Co_{0.10}Mn_{0.10}O_2$ cathode material operating at high potentials. *J. Energy Chem.* **41**, 135 (2020).

40. Zhang, J. *et al.* Unraveling the intra and intercycle interfacial evolution of Li_6PS_5Cl-based all-solid-state lithium batteries. *Adv. Energy Mater.* **10**, 1903311 (2020).

41. Friedrich, F. *et al.* Capacity fading mechanisms of NCM-811 cathodes in lithium-ion batteries studied by X-ray diffraction and other diagnostics. *J. Electrochem. Soc* **166**, A3760 (2019).

42. Tan, D. H. S. *et al.* Elucidating reversible electrochemical redox of Li_6PS_5Cl solid electrolyte. *Energy Lett.* **4**, 2418 (2019).

43. Li, J. *et al.* Study of the failure mechanisms of $LiNi_{0.8}Mn_{0.1}Co_{0.1}O_2$ cathode material for lithium ion batteries. *J. Electrochem. Soc* **162**, A1401 (2015).

44. Li, J., Shunmugasundaram, R., Doig, R. & Dahn, J. R. In situ x-ray diffraction study of layered Li–Ni–Mn–Co oxides: effect of particle size and structural stability of core–shell materials *Chem. Mater.* **28**, 162 (2016).

45. Zhu, Y., He, X. & Mo, Y. Origin of outstanding stability in the lithium solid electrolyte materials: insights from thermodynamic analyses based on first-principles calculations. *ACS Appl. Mater. Interfaces* **7**, 23685 (2015).

46. Richards, W. D. *et al.* Interface stability in solid-state batteries. *Chem. Mater.* **28**, 266 (2016).

47. Banerjee, A. *et al.* Revealing nanoscale solid–solid interfacial phenomena for long-life and high-energy all-solid-state batteries. *ACS Appl. Mater. Interfaces* **11**, 43138 (2019).

48. Jung, R. *et al.* Oxygen release and its effect on the cycling stability of $LiNi_xMn_yCo_zO_2$ (NMC) cathode materials for Li-ion batteries. *J. Electrochem. Soc* **164**, A1361 (2017).

49. Strehle, B. *et al.* The role of oxygen release from Li-and Mn-rich layered oxides during the first cycles investigated by on-line electrochemical mass spectrometry. *J. Electrochem. Soc* **164**, A400 (2017).

50. Jung, R. *et al.* Chemical versus electrochemical electrolyte oxidation on NMC111, NMC622, NMC811, LNMO, and conductive carbon. *J. Phys. Chem. Lett.* **8**, 4820 (2017).

51. Wandt, J., Freiberg, A. T. S., Ogrodnik, A. & Gasteiger, H. A. Singlet oxygen evolution from layered transition metal oxide cathode materials and its implications for lithium-ion batteries. *Mater. Today* **21**, 825 (2018).

52. Rodríguez-Carvajal, J. FullProf. CEA/Saclay, France (2001).

Chapter 4. Summary

In this thesis, I present issues on the composite cathode interface in all-solid-state batteries when carbon conductive agents are introduced for designing high-power density and all-solid-state batteries are exposed to calendar aging at wide range of storage temperatures. The contents include (i) dilemma in constructing ASSB concerning the conductive agent, which provides the electronic pathway but simultaneously promotes the degradation of the electrolyte, and (ii) investigation on the reliability of Li_6PS_5Cl-based ASSB system in practically harsh but plausible storage conditions.

In the first part, I found out that the introduction of carbon additives in composite cathode induces a large polarization during charging and discharging, followed by the decreased initial capacity along with an unusual voltage slope at around 2.6 V vs Li/Li^+. Moreover, I verified that the degradation of the electrochemical performance of the carbon-containing cathode composite is correlated with the severe impedance increase at the cathode interface during cycles. The surface analysis of the composite cathode with carbon revealed that the oxidation of sulfur occurs in LGPS during charging, involving the severe loss of the lithium-sulfur bonding and the formation of sulfur-sulfur bonding, which is indicative of the degradation of LGPS. It is believed that the deterioration of LGPS with carbon that triggers the electrochemical reaction of LGPS increases the interfacial impedance in the composite cathode by interfering the Li^+ pathway.

Furthermore, such Li^+ pathway interference induces large polarization and serious capacity loss in ASSBs. This work shows that a dilemma in constructing ASSB concerning the conductive agent, which provides the electronic pathway but simultaneously promotes the degradation of the electrolyte. Therefore, optimizing the amount of carbon conductive agents or finding a suitable conductive agent with a minimal influence on the electrolyte is essential in designing high power density ASSBs employing sulfide electrolytes.

In the second part, I studied the reliability of Li_6PS_5Cl-based ASSB system in practically harsh but plausible storage conditions, and found out that a substantial deterioration of ASSB can occur after the high-temperature storage as low as 70 °C. From the extensive characterizations, we confirmed that this degradation is correlated with the corrosion of the cathode/Li_6PS_5Cl interface, which is accompanied by SO_x gas evolution, developing a detrimental porous interface structure that results in the physical particle-to-particle disconnect in the composite cathode. It indicates that the stability of the solid electrolyte, which has been believed to be excellent, needs to be carefully revisited at various practical operational conditions for actual applications in ASSBs. In conclusion, my thesis suggests that future research efforts should be placed in developing effective strategies to overcome various issues with ASSBs in real-world environments in order to successfully mount ASSBs in EVs.

Abstract in Korean

초록

에너지 저장 시스템 중, 충전식 리튬 이온 배터리는 저렴한 비용, 높은 에너지 밀도, 전력 용량 및 안정적인 사이클을 보장하여 수십 년 동안 소형 전자 장치에 가장 성공적인 배터리 시스템이었다. 최근 배터리 시스템의 적용이 소형 전자기기에서 전기자동차(EV)와 같은 대형 전자기기로 확대됨에 따라 안전하고 에너지 밀도가 높은 배터리를 찾는 것이 중요한 과제가 되었다. 특히, 기존의 리튬이온 이차전지에 유기 액체전해질이 존재하면 폭발에 의해 사용자의 안전이 위협받고, 대형 전지의 경우 생명을 위협할 수 있다.

최근, 불연성 고체 전해질을 사용하는 전고체배터리는 안전성 측면에서 전기 자동차의 가장 유망한 후보 중 하나로 간주된다. 높은 이온 전도성을 가진 새로운 고체 전해질에 대한 광범위한 연구는 전고체전지 개발에서 지난 수십 년 동안 수행되었습니다. 그 중 최근에 발견된 황화물계 전해질은 이온전도도가 상용 유기 액체 전해질과 유사한 수준에 도달할 수 있어 최근 전고체전지가 차세대배터리로 각광받고 있다. 더욱이, 황화물의 기계적 성질은 일반적으로 전극의

다른 구성요소와 상당히 양호한 물리적 접촉을 제공하여 고체 구성요소 사이의 큰 접촉 저항을 완화한다. 따라서 고용량 리튬 금속의 적용과 다용도 폼 팩터를 활용하여 지속적인 노력을 통해 최근 몇 년 동안 고에너지 밀도 전고체전지의 급속한 개발은 전기차용 대용량 전지에서 전고체배터리의 상용화에 더욱 가까워졌다. 그러나 전기차에 전고체전지를 성공적으로 장착하기 위해서는 고속 충전을 위한 고출력 밀도를 달성하고 다양한 온도에서 캘린더 노화 특성을 조사하는 것이 핵심 임무가 될 것이다. 이 논문에서는 황화물 전해질을 사용하는 전고체 배터리가 고출력 밀도를 위해 설계될 때와 광범위한 보관 온도에서 캘린더 노화에 노출될 때 전고체 배터리의 복합 음극 계면에 대한 문제를 제시한다.

2 장에서는 고출력 밀도의 전고체전지를 구현하는데 있어 카본 전도제를 도입하게 되는데 전기 경로를 제공하지만 동시에 황화물 전해질의 분해를 촉진하는 카본 전도제에 관한 전고체전지 구성의 딜레마를 제기한다. 복합 양극에 탄소 첨가제를 포함하면 충전 및 방전 중에 큰 분극이 발생하고 초기 용량이 감소한다는 것을 발견하였다. 또한, 탄소 함유 양극 복합체의 전기화학적 성능 저하가 사이클 동안 양극 계면에서 심각한 임피던스 증가와 상관관계가 있음을 발견했다. 따라서 황화물 전해질을 사용하는 고전력 밀도 ASSB 를 설계하기

위해서는 탄소 전도제의 양을 최적화하거나 전해질에 최소한의 영향을 미치는 적절한 전도제를 찾는 것이 필수적이다.

3 장에서는 Li_6PS_5Cl 고체 전해질과 $LiNi_{0.8}Co_{0.1}Mn_{0.1}O_2$(NCM811) 음극으로 구성된 가장 대표적인 전고체전지 시스템의 캘린더 노화 특성을 조사하여 다양한 실외 조건에서 전고체전지의 실제 보관 조건을 모방하여 전고체전지의 성능이 (i) 실외 온도, (ii) 연장된 저장 기간 및 (iii) 충전상태에 노출되었을 때 어떻게 유지/변경되는지 주의 깊게 조사하였다. Li_6PS_5Cl-NCM811 전고체전지가 상혼 혹은 저온에서 성능을 훌륭하게 잘 유지할 수 있음을 보여주었고, 이는 액체 전해질을 포함하는 LIB 와 비교해보았을 때 전지의 캘린더 노화 특성을 능가한다. 반면에 전고체전지의 상당한 열화는 고온 보관 후 관찰되며 전지저항의 상당한 증가와 방전용량의 거의 절반 미만으로 용량 감소를 동반하여 명확한 대조를 보여준다. 본 연구를 통해 전고체전지를 전기차에 성공적으로 탑재하기 위해 실제 환경에서 전고체전지 복합양극의 다양한 문제를 알아보았고 이러한 문제들을 극복할 수 있는 효과적인 전략을 개발하는데 향후 연구에 지침서가 될 수 있을 거라 생각한다.

주요어 : 에너지 저장장치, 배터리, 전고체배터리, 복합양극계면, 황화물계 고체전해질

학번 : 2016-20805